Replacement reactions and deformation by dissolution and precipitation processes in amphibolites

Francesco Giuntoli [a*], Luca Menegon [a], Clare J. Warren [b]

[a] School of Geography, Earth and Environmental Sciences, Plymouth University, Plymouth PL4 8AA, UK (francesco.giuntoli@gmail.com)

[b] School of Environment, Earth and Ecosystem Sciences, Faculty of Science, Technology, Engineering and Mathematics, The Open University, Walton Hall, Milton Keynes, MK7 6AA, UK

Short title: dissolution-precipitation in amphibolites

Abstract

The deformation of the middle to lower crust in collisional settings occurs via deformation mechanisms that vary with rock composition, fluid content, pressure and temperature. These mechanisms are responsible for the accommodation of large tectonic transport distances during nappe stacking and exhumation. Here we show that fracturing and fluid flow triggered coupled dissolution-precipitation and dissolution-precipitation creep processes, which were responsible for the formation of a mylonitic microstructure in amphibolites. This fabric is developed over a crustal thickness of >500 m in the Lower Seve Nappe (Scandinavian Caledonides). Amphibolites display a mylonitic foliation that wraps around albite porphyroclasts appearing dark in panchromatic cathodoluminescence. The albite porphyroclasts were dissected and fragmented by fractures preferentially developed along the (001) cleavage planes, and display lobate edges with embayments and peninsular features. Two albite/oligoclase generations, bright in cathodoluminescence, resorbed and overgrew the porphyroclasts, sealing the fractures. Electron backscattered diffraction shows that the two albite/oligoclase generations grew both pseudomorphically and topotaxially at the expenses of the albite porphyroclasts and epitaxially around these. These two albite/oligoclase generations also grew as neoblasts elongated parallel to the mylonitic foliation. The amphibole crystals experienced a similar microstructural evolution, as evidenced by corroded ferrohornblende cores surrounded by ferrotschermakite rims that preserve the same crystallographic orientation of the cores. Misorientation maps highlight how misorientations in amphibole are related to displacement along fractures perpendicular to its c-axis. No crystal plasticity is observed in either mineral species. Plagioclase and amphibole display a crystallographic preferred orientation that is the result of topotaxial growth on parental grains and nucleation of new grains with a similar crystallographic orientation. Amphibole and plagioclase thermobarometry constrains the mylonitic foliation development to the epidote amphibolite facies (~600°C, 0.75-0.97 GPa). Our results demonstrate that at middle to lower crustal levels the presence of H_2O-rich fluid at grain boundaries facilitates replacement reactions by coupled

dissolution-precipitation and favours deformation by dissolution-precipitation creep over dislocation creep in plagioclase and amphibole.

Keywords

Replacement reactions, dissolution-precipitation processes, Caledonides, electron backscatter diffraction, X-ray mapping.

1. INTRODUCTION

The thermo-mechanical properties of the middle to lower crust exert a fundamental control on the structure of orogenic belts, and on the amount and style of shortening during continental collision (e.g. Jackson, Austrheim, McKenzie, & Priestley, 2004; Mouthereau, Watts, & Burov, 2013). In particular, how strain is distributed vertically and horizontally in orogenic belts is one of the more important questions in crustal dynamics, and one that can be addressed by investigating the deformation mechanisms associated with the accumulation of hundreds of km tectonic transport distances along thrust faults during mountain building processes (e.g. Fusseis & Handy, 2008; Gilotti, 1989; Mouthereau, Lacombe, & Vergés, 2012; Northrup, 1996; Royden, 1996).

In particular, the deformation processes and rheology of mafic shear zones are the subject of considerable debate, because their main mineral constituents (e.g. plagioclase, amphibole, clinopyroxene) are expected to be rheologically strong at middle to lower crustal conditions (e.g. Bürgmann & Dresen, 2008). Thus, the weakening of mafic assemblages along major thrust faults developed at middle to lower crustal conditions seems to critically depend on the occurrence of metamorphic reactions, which can result in the formation of rheologically weaker phases, or in the formation of fine-grained material able to deform by grain size sensitive creep, or in both (e.g. Rutter & Brodie, 1992; Brander, Svahnberg, & Piazolo, 2012; Okudaira, Shigematsu, Harigane, & Yoshida, 2017). Furthermore, the presence of H_2O-rich fluid at the grain boundary typically facilitates dissolution and precipitation processes, which have been identified as the main deformation

mechanisms in different mid-crustal lithologies and up to high temperature and high pressure conditions (Carmichael, 1969; Giuntoli, Lanari, & Engi, 2018; Gratier, Dysthe, & Renard, 2013; Imon, Okudaira, & Fujimoto, 2002; Imon, Okudaira, & Kanagawa, 2004; McAleer et al., 2017; Menegon, Pennacchioni, & Spiess, 2008; Mukai, Austrheim, Putnis, & Putnis, 2014; Putnis, 2009; Rutter, 1983; Stokes, Wintsch, & Southworth, 2012; Wassmann & Stöckhert, 2013; Wassmann, Stöckhert, & Trepmann, 2011; Wintsch & Yi, 2002). Two main dissolution and precipitation processes can be distinguished: coupled dissolution-precipitation and dissolution-precipitation creep. Coupled dissolution-precipitation results in the pseudomorphic (maintaining the size and shape of the pre-existing phase) and topotaxial (using the orientation of the pre-existing phase) replacement of a parent phase by a product phase from a reaction interface (e.g. Putnis, 2002; Ruiz-Agudo, Putnis, & Putnis, 2014). Dissolution-precipitation creep includes the transport of the chemical constituents from the dissolution sites, of locally high normal stress, to the precipitation site, of locally low normal stress (e.g. Imon et al., 2002; Imon et al., 2004; Mukai et al., 2014; Wassmann et al., 2011). Both processes invariably require the presence of a fluid.

Porosity is another essential requirement for the operation of dissolution and precipitation processes, as it provides the necessary fluid pathways. Porosity may develop during replacement reactions due to molar volume differences between the dissolved and the precipitated minerals (Engvik, Putnis, Gerald, & Austrheim, 2008), or from dehydration reactions and associated fracturing (Plumper, John, Podladchikov, Vrijmoed, & Scambelluri, 2017). Other porosity-generating mechanisms in metamorphic environments include dilatancy at grain boundaries (Tullis, Yund, & Farver, 1996), fracturing (e.g. Brander et al., 2012), and creep cavitation in fine-grained ultramylonites deforming by grain size sensitive creep (Fusseis, Regenauer-Lieb, Liu, Hough, & De Carlo, 2009; Menegon, Fusseis, Stünitz, & Xiao, 2015).

Here we show that mineral reactions and deformation in amphibolites occurred mainly by coupled dissolution-precipitation and dissolution-precipitation creep at epidote-amphibolite facies conditions,

and that fracturing was the most efficient porosity-generating mechanism assisting deformation. Metamorphism and deformation in the amphibolites resulted in the development of a > 500 m thick mylonitic foliation during Caledonian nappe thrusting.

2. GEOLOGICAL SETTING

The Scandinavian Caledonides developed due to the closure of the Iapetus Ocean in the Ordovician, and the subsequent subduction and continent collision of the Baltica plate below the Laurentia plate in the Silurian to early Devonian (e.g. Gee, Fossen, Henriksen, & Higgins, 2008; Roberts, 2003; Roberts & Gee, 1985; Stephens, 1988). In the Scandinavian Caledonides, tectonic units were transported up to 400 km to the east (Gayer, Rice, Roberts, Townsend, & Welbon, 1987; Gee, 1975; Gee, Juhlin, Pascal, & Robinson, 2010; Rice & Anderson, 2016; Roberts & Gee, 1985) as a result of the collision, creating a nappe stack of several allochthons units on top of Autochthons Baltic Shield (Figure 1a-b). After emplacement, the nappe stack was folded into north-trending synforms and antiforms, possibly related to the crustal extension and normal faulting occurring during the latest orogenic phases (Bergman & Sjöström, 1997). By virtue of their deep erosional level, the internal parts of the Scandinavian Caledonides expose middle and lower crustal sections involved in subduction-exhumation history and nappe stacking.

The Scandinavian Caledonides are subdivided, from top to bottom, into an Uppermost Allochthon, an Upper Allochthon, a Middle Allochthon, and a Lower Allochthon based on tectonostratigraphy (Figure 1; Gee & Sturt, 1985; Strand & Kulling, 1972; Strömberg et al., 1984). The Middle Allochthon, the target of this study, includes several basement units and associated metasediments representing the outermost Baltica margin and possibly including units derived from an ocean-continent transition zone (e.g. Andréasson, 1994; Gee et al., 2008; Gee, Janák, Majka, Robinson, & van Roermund, 2013; Roberts, 2003; Stephens, 1988). The upper tectonic unit of the Middle Allochthon is the Seve Nappe Complex (SNC; e.g. Sjöström, 1983), which, in the central Scandes,

outcrops over a N-S distance of ~1000 km and an W-E distance of ~200 km (Figure 1; Andréasson, 1994).

In the Jämtland region, the SNC can be further subdivided into Lower, Middle and Upper Seve Nappe by the presence of internal thrust sheets (Zachrisson & Sjöstrand, 1990). The Lower Seve Nappe is mainly composed of micaschists, quartzites and metapsammites with gneisses, metabasics and with minor peridotites and serpentinites (Figure 1c). The Middle Seve Nappe is composed of similar lithotypes, but overprinted by a pervasive migmatization. Several parts of the Lower- and Middle Seve preserve evidence of high pressure (HP) to ultrahigh pressure (UHP-) metamorphism (summary in Figure 4 of Klonowska, Janák, Majka, Froitzheim, & Kośmińska, 2016) spanning from ~1.1 GPa and 600°C up to 4 GPa and 800°C, within the stability field of coesite and diamond (Brueckner & van Roermund, 2004; Gilio, Clos, & van Roermund, 2015; Janák, van Roermund, Majka, & Gee, 2013; Klonowska et al., 2016; Klonowska et al., 2017; Majka et al., 2014; Van Roermund, 1985, 1989). The HP-UHP metamorphism is the manifestation of the Ordovician subduction of the SNC (Brueckner & Van Roermund, 2007; Ladenberger et al., 2013; Root & Corfu, 2012). It is worth noting that to date, no evidence of (U)HP metamorphism has been recorded in the Lower Seve Nappe in the central Jämtland. In the Middle Seve Nappe, the granulite and amphibolite facies metamorphism appears to postdate the HP-UHP stage, and produced partial melting at 442–436 Ma (Ladenberger et al., 2013). A recent study has related the amphibolite facies metamorphic "stage" to the exhumation and lateral extrusion of the SNC (Grimmer, Glodny, Drüppel, Greiling, & Kontny, 2015). In the Lower Seve Nappe, a pervasive amphibolite facies foliation overprints the (U)HP fabric where present; where not present it represents the main metamorphic fabric. In the Åreskutan area, the amphibolite facies metamorphic stage was constrained at 550°C and 0.2 to 0.5 GPa (Arnbom, 1980).

The "Collisional Orogeny in the Scandinavian Caledonides (COSC-1)" borehole (Lorenz et al., 2015; see location in Figure 1b-c) is located in the central Jämtland region, near Åre (Sweden). The drill core provides an almost complete section (recovery rate higher than 99%) through the Lower Seve

Nappe. In detail, the core comprises alternating layers of felsic gneisses, calc-silicates and amphibolites displaying narrow (mm-cm) and localized shear zones from the surface down to 1700 m (Hedin et al., 2016). The rocks show strongly deformed fabrics from 1700 m to 2500 m (the end of the core; Lorenz et al., 2015), with the development of mylonitic fabrics. The lowermost portion of the core is composed of strongly deformed metasediments. Acoustic televiewer data indicates that the foliation is generally shallow and trends N-S, but there are remarkable exceptions, where the foliation has dips to the E or W with angles >50°, related to recumbent folds and boudinage (Wenning et al., 2017).

3. METHODS

3.1 Scanning electron microscopy (SEM)

All the SEM analyses were performed on carbon-coated polished thin sections cut perpendicular to the foliation and parallel to the stretching lineation of the sample. Backscattered electron (BSE) and cathodoluminescence (CL) analyses were performed at the Open University (UK), using an FEI Quanta 200 three-dimensional SEM on carbon coated thin sections. Analyses were conducted under high vacuum, using an accelerating voltage of 10 kV, a beam current of 3.3 nA, a working distance of 13 mm, and an electron source provided by a tungsten filament. The panchromatic CL detector used is a Centaurus Deben with a photo multiplier tube (Hamamatsu R316) characterized by sensitivity in the range of 400-1200nm.

Electron backscattered diffraction (EBSD) analyses were conducted with a Jeol-7001FEG SEM at the Electron Microscopy Centre, Plymouth University (UK). EBSD patterns were acquired with a 70° tilted sample geometry, 20 kV accelerating voltage, 18-23 mm working distance and 1.3-1.7 µm step size. Diffraction patterns were automatically indexed using AZtec (Oxford Instruments). The indexing match units used for the analysed phases were “anorthite” (Laue group -1) for albite and oligoclase, and “hornblende” (Laue group 2/m) for tschermakite-ferrotschermakite. Both match units

156 were taken from the American Mineralogist database. Raw maps were processed with HKL Channel
157 5 (Oxford Instruments), using the noise reduction procedure tested by Prior, Wheeler, Peruzzo,
158 Spiess, and Storey (2002). Wild spikes were removed, and un-indexed points were replaced by the
159 average orientation of the neighbour points. Grains smaller than 3 times the step size were not
160 considered in the analysis. The mean angular deviation values were 0.3 for amphibole and 0.4-0.6 for
161 plagioclase; the raw indexing rate ranged between 90% and 95%. Crystallographic directions were
162 plotted on pole figures (upper and lower hemisphere of the stereographic projection), with X parallel
163 to the stretching lineation and Z parallel to the pole of the mylonitic foliation. The grain orientation
164 spread maps (GOS maps) were calculated as the average misorientation between every pixel in the
165 grain and the grain's average orientation.

166 **3.2 Electron probe micro-analyser (EPMA)**

167 EPMA analyses were conducted at the Open University (UK), using a Cameca SX100 connected to
168 five spectrometers. Wavelength dispersive spectrometers (WDS) were used for both spot analyses
169 and X-ray maps, the latter acquired following the procedure of Lanari et al. (2013). Spot analyses
170 were acquired first for each mineral phase, before performing the X-ray maps on the same area. Spot
171 analyses were performed with 20 KeV accelerating voltage, 20 nA specimen current and 2 μm beam
172 diameter. Ten oxide compositions were measured, using natural standards: K-feldspar (SiO_2, Al_2O_3,
173 K_2O), bustamite (CaO, MnO), hematite (FeO), forsterite (MgO), jadeite (Na_2O), rutile (TiO_2), apatite
174 (P_2O_5). A ZAF matrix correction routine was applied; uncertainty on major element concentrations
175 was <1%. X-ray maps were acquired with 15 KeV accelerating voltage, 100 nA specimen current,
176 dwell times of 70-100 ms and step size of 5 μm. Ten elements (Si, Ti, Al, Fe, Mn, Mg, Na, Ca, K and
177 P) were measured at the specific wavelength in two series. Intensity X-ray maps were standardized
178 to concentration maps of oxide weight percentage using spot analyses as internal standard. X-ray
179 maps were processed using XMapTools 2.2.1 (Lanari et al., 2014).

180 **3.3 Geothermobarometry**

3.3.1 Amphibole-plagioclase thermobarometry

Temperature (T) was estimated using Holland and Blundy (1994) geothermometer. In detail, the Holland and Blundy (1994) thermometer is based on element exchange between amphibole and plagioclase pairs in equilibrium; the calibration reaction edenite + albite = richterite + anorthite was constrained from experimental and natural data for silica-saturated and silica-rich igneous and metamorphic rocks in the range of 0.1-1.5 GPa and 400-1000 °C.

Pressure (P) was estimated using two geobarometers: Bhadra and Bhattacharya (2007) and Anderson and Smith (1995). The former is based on element distribution between amphibole and plagioclase pairs in equilibrium. Experimental data were conducted on silica-saturated assemblages in the P-T range of 0.1-1.5 GPa and 650-950 °C and on the reaction tremolite + tschermakite + 2 albite = 2 pargasite + 8 quartz. The latter is based on the increase of Al content in hornblende with increasing P and is calibrated on experimental data at 675 and 760 °C, accounting for the effects of T and f_{O_2}. P and T were calculated using the Plagioclase–Hornblende Thermobarometry spreadsheet (Anderson, Barth, Wooden, & Mazdab, 2008) and the spreadsheet of Wallis, Phillips, and Lloyd (2014) (the latter was used to derive P from the calibration of Bhadra & Bhattacharya, 2007).

3.3.2 Chlorite+Quartz+H2O thermometry

Chlorite+Quartz+H_2O thermometry was performed using the program CHLMICAEQUI (Lanari, 2012). The crystallization temperature of chlorite and the XFe^{3+} were computed at a fixed pressure of 0.7 GPa in the temperature range of 100 to 550°C from the convergence of four equilibria involving five chlorite end-members, quartz and H_2O (Lanari et al., 2012; Vidal, Lanari, Munoz, Bourdelle, & De Andrade, 2016) using standard state properties and solid solution models of Vidal, Parra, and Vieillard (2005; 2006).

4. RESULTS

4.1 Petrography and microstructure

In the middle and lower portions of the COSC-1 borehole (~1500-2300 m deep), amphibolites show a mylonitic foliation. The studied sample (International Geological Sample Number: ICDP5054EX8E601) was extracted from a depth of 2206.97 metres from the surface and is similar to several amphibolite samples present between ~1600 and ~2300 m of depth. In this sample the mylonitic foliation is subhorizontal, it wraps around plagioclase porphyrocrysts and is defined by amphibole, plagioclase (with smaller grain size, details in the following), chlorite, quartz, epidote and ilmenite (Figure 2). Quartz and calcite occur mainly in veins subparallel to the mylonitic foliation or as fine grains dispersed in the mylonitic foliation, typically along the phase boundaries between plagioclase and amphibole.

Plagioclase is present as zoned porphyrocrysts (up to 0.5-1 cm in size) wrapped by the mylonitic foliation, and as finer (up to hundreds of μm in size) albite/oligoclase grains elongated parallel to the mylonitic foliation (aspect ratios up to ~ 5; mean ~ 2). Plagioclase porphyrocrysts have albite cores that appear turbid due to abundant fine-grained (up to 30 μm in size) inclusions of ilmenite, rutile and epidote. Ilmenite crystals are also included with bigger grain size (100 microns in size); quartz is present as inclusions with variable grain size (tens to hundreds of μm in size; Figures 3 and 4). The inclusions locally define a rotated internal foliation (upper plagioclase porphyrocryst in Figure 3a). These cores are porphyroclastic, and are cut by fracture systems and some are dismembered parallel to the foliation (see details in section 4.2). The cores are always surrounded by albite/oligoclase rims. Pores are evident in the albite/oligoclase rims: they are few microns in size and occur in trails parallel to fracture systems that dissect the plagioclase core (Figure 4). Several mineral inclusions also occur along such trails, ranging from a few microns to tens of microns in size. These are muscovite, epidote and calcite, with rare Ba-rich muscovite (Figure 4). Such inclusions confer a turbid aspect to plagioclase rim in plane-polarized light micrographs (Figure 3a, Table 1).

Amphibole is pleochroic, with absorption colours ranging from light brown to dark green-blue; in some bigger crystals absorption colours highlight a paler core and a darker rim. Amphibole displays

the C-axis parallel to the stretching lineation and a maximum grain size of >1 mm. Chlorite has a pleochroism varying from light yellow to light green, a negative optical sign and grain size similar to the amphibole. Asymmetric pressure shadows around plagioclase porphyroclasts indicate both dextral and sinistral sense of shear. In these pressure shadows amphibole, albite/oligoclase grains and chlorite crystallize intergrown and elongated parallel to the mylonitic foliation. C' planes display a dominant sinistral sense of shear and are defined by the same minerals found along the mylonitic foliation (Figures 2, 3a-b). Opaque minerals include mostly ilmenite, up to 1 mm in size, with minor magnetite and pyrite. Ilmenite crystals are elongate and lie parallel to the mylonitic foliation.

4.2 Microstructure and chemistry of plagioclase

BSE images highlight two plagioclase generations: dark cores with an albitic composition (Pl1) are surrounded by brighter plagioclase rims with higher anorthite content (Pl2 and Pl3, as defined based on chemistry in the next paragraph; Figures 3c and 4). Furthermore, the cores are cut by fractures filled with plagioclase with the same composition as the plagioclase rims. The distinction of these plagioclase generations is more evident in the CL images, where plagioclase cores appear moderately luminescent and are surrounded by bright plagioclase rims (Figure 3d). The fractures dissecting the cores are as bright as the plagioclase rims. The plagioclase cores (Pl1) are locally fragmented and display lobate edges and embayments that are typically surrounded by bright plagioclase (Figures 3d, 7a and 8b). In some areas, the plagioclase rims can be further subdivided into two generations based on the brightness of their CL response: a brighter plagioclase generally surrounded by a darker one (Pl2 and Pl3, respectively).

Compositional maps of plagioclase display a perfect match with the CL images (Figure 3e). The maps highlight three plagioclase compositions, numbered from the older to the younger: Pl1 (XAn 0-0.05), Pl2 (XAn 0.13-0.25), Pl3 (XAn 0.05-0.13; Figures 5a, 7b, Table 2). The plagioclase core (Pl1) has an albite composition and is overgrown by the two albite/oligoclase rims (Pl2 and Pl3). Pl2 is present only locally and is overgrown by Pl3, as shown in the top right corner of Figure 3e.

255 Furthermore, Pl3 seals the fractures inside Pl1. Pl1 forms porphyroclasts wrapped by the mylonitic
256 foliation, whereas Pl2 and Pl3 occur in the pressure shadows of Pl1.

257 **4.3 Microstructure and chemistry of amphibole and chlorite**

258 Compositional maps of amphibole crystals display corroded cores, higher in Mg#
259 (Mg#=Mg/(Fe^{2+}+Mg); Amp1: Mg# 0.5-0.44, Si apfu 7-6.5), and rims, lower in Mg# (Amp2: Mg#
260 0.44-0.36, Si apfu 6.5-6.1; Figures 3f and 5b, Table 2). Based on the classification of Leake et al.
261 (1997) the Amp1 is at the compositional boundary between tschermakite-ferrotschermakite-
262 magnesiohornblende-ferrohornblende; Amp2 is a ferrotschermakite (Figure 5c). There are local
263 exceptions to this zoning pattern, in which the two peripheral areas have higher Mg# (Figure 9c).
264 Amp2 and Pl3 grains displaying mutual intergrowths and elongation parallel to the foliation (Figure
265 3 c-f)

266 Chlorite is characterized by a homogeneous Mg# (Mg# 0.59-0.56, Chl1), except along grain
267 boundaries and the C' planes, where some lower values are visible (Mg# 0.55-0.52, Chl2; Figure 5c,
268 Table 3). Chl1 grains occur as intergrown with Pl3 and Amp2 along the mylonitic.

269 **4.4 Amp-Pl thermobarometry**

270 Thermometric estimates for the Pl1 and Amp1 pair yield 400°C; thermobarometric estimates for the
271 Pl2 and Amp1 pair and the Amp2 and Pl3 pair yield 615°C and 0.97 GPa and 605°C and 0.74 GPa
272 respectively (±50 °C ±0.2 GPa, Table 4; see Section 5.1 for discussion on the Pl and Amp growth
273 zones that we consider to be in equilibrium).

274 **4.5 Chlorite+Quartz+H_2O thermometry**

275 Chlorite+Quartz+H_2O thermometry was performed on the two different chlorite groups, Chl1 and
276 Chl2 (Figure 5c), at a fixed pressure of 0.7 GPa. Chl1 displays two peaks in the T-frequency diagram
277 (Figure 6a): one close to the T limit of the thermometer (550°C-450°C) and one at lower T (400°C-

250°C). Chl2 yields T in the range of 200-350°C, with a peak at ~250°C (Figure 6b), with only one grain yielding a higher T (~500°C).

4.6 EBSD analysis

Figures 7-8 show the results of EBSD analysis of two microstructural domains (see Figures 2 and 3 for the location of EBSD maps): domain 1 includes a plagioclase porphyrocryst with a core of Pl1 composition rimmed by Pl2 and Pl3 compositions. The porphyroclast Pl1 is cut by a network of intracrystalline microfractures oriented NW-SE and filled with Pl2-Pl3. Domain 1 also includes clusters of amphibole and plagioclase grains around the plagioclase porphyrocryst (Figure 7). Domain 2 contains an aggregate of amphibole grains, mostly elongate parallel to the foliation, and several grains of plagioclase showing a core-and-rim zoning in CL images (Figure 8).

The comparison between EBSD maps, CL images and compositional maps shows that the Pl1 porphyroclasts, which EBSD identifies as one individual grain (i.e. it does not contain high-angle boundaries with misorientation > 10°), actually include areas with Pl2 and Pl3 compositions, which maintain the original crystal shape and crystallographic orientation of Pl1 (Figures 7 and 8). The internal distortion of the compositionally zoned porphyrocrysts, as evaluated with the GOS, is rather low (GOS values lower than 2°: Figures 7c and 8e). Low-angle boundaries (misorientations 2-10°) are preferentially distributed along the microfracture. The analysis of local misorientations within Pl1 cores indicates that Pl2 and Pl3 areas have misorientations of up to 2° with respect to the Pl1 cores (Figure 7d). Higher misorientations (up to 3°) are found in the plagioclase porphyrocryst of the domain 2 (Figure 8d).

In domain 1, the compositionally zoned plagioclase porphyrocryst is surrounded by Pl2-Pl3 grains that range in size between 30 and 200 μm, delimited by high-angle boundaries with misorientation > 10° from the porphyrocryst. The Pl2 and Pl3 grains have mean GOS values lower than 1°, with one maximum value of 4°.

302 Amphibole generally shows GOS values lower than 2°, with a few maxima of up to 7° (Figures 7e,
303 8g, 9d). Misorientations progressively increase towards fractures perpendicular to the crystal
304 elongation and, locally, towards very few low angle boundaries oriented subparallel to the crystal
305 elongation (Figures 7f, 8h, 9f). The misorientation profile in Figure 9e highlights a jump in
306 misorientation of up to 7° across the low angle boundary.

307 The crystallographic orientation of the new grains of Pl2 and Pl3 displays a variable degree of overlap
308 with the one of the Pl1 core that they overgrow (Figures 10a-b and 11a-b). In some cases, all the new
309 grains inherit the crystallographic orientation of the Pl1 core (Figure 10a-b), whereas in other cases,
310 the overlap is more limited and the new grains show a significant dispersion of crystallographic
311 directions with respect to the Pl1 cores (Figure 11). The crystallographic inheritance is more evident
312 if we consider the crystallographic orientation of the Pl2-Pl3 grains in direct contact with the Pl1 core
313 (Figures 10a and 11b). The Pl2-Pl3 grains dispersed in the mylonitic matrix show a wide range of
314 crystallographic orientations, which do not necessarily overlap with those of the Pl1 cores included
315 in the map (Figures 10b and 11a). EBSD analysis also shows that the most common fracture set in
316 the Pl1 porphyroclasts is parallel to the (001) plane, which is a perfect cleavage plane in plagioclase
317 (Figure 11a).

318 Amphibole has a strong CPO, with the (100) and [001] subparallel to the foliation and to the stretching
319 lineation, respectively (Figures 10c and 11c). The misorientation angle distribution of amphibole
320 displays the strongest peaks between 2° and 25° and around 50° and 180°, with higher values for the
321 correlated pairs (Figure 11d). The misorientation axes of amphibole, plotted in crystal coordinates,
322 show maxima around the c-axis for misorientations up to 30°, which, in sample coordinates, is
323 oriented subparallel to the stretching lineation of the mylonite (Figure 11d).

324 5. DISCUSSION

325 5.1 P-T conditions of metamorphism and deformation

326 The Anderson and Smith (1995) geobarometer calibration was based on rocks that equilibrated in the
327 presence of melt. There is no evidence of melt in our sample, therefore we favour the pressure results
328 from Bhadra and Bhattacharya (2007; Table 4). However, we kept both results, as the Plagioclase–
329 Hornblende Thermobarometry spreadsheet (Anderson et al., 2008) that we used to compute P and T
330 utilises a convergence between the results of Anderson and Smith (1995) geobarometer and Holland
331 and Blundy (1994) geothermometer. As a test, we used the Bhadra and Bhattacharya (2007) P results
332 as input for the Holland and Blundy (1994) geothermometer and we obtained coincident T results,
333 within error.

334 The oldest metamorphic stage preserved in the sample is represented by the albite cores (Pl1) with
335 their oriented inclusions of epidote, ilmenite and rutile. In particular, rutile inclusions suggest
336 relatively high pressure, but the coexistence with albite crystals would constrain the maximum
337 pressure of this metamorphic stage below the albite breakdown reaction (albite = jadeite + quartz;
338 Newton & Smith, 1967). However, the exact conditions of this first metamorphic stage were not
339 constrained in this study.

340 The microstructural relationships between Pl1 and Amp1 are equivocal, therefore it is difficult to
341 prove that they grew in equilibrium. Their compositions suggest that had they grown in equilibrium,
342 they would have crystallised at 400°C (Table 4). These results, however, are far away from the lower
343 limits of the calibration of Bhadra and Bhattacharya (2007; 650-950°C) and Anderson and Smith
344 (1995; 675–760 °C): for this reason, pressures were not computed for the Amp1-Pl1 pairs.
345 Furthermore, Pl1 is out of the compositional range of the Bhadra and Bhattacharya (2007)
346 equilibration (Table 10 of that contribution).

347 Within uncertainty, the T results of Amp1-Pl2 and Amp2-Pl3 pairs lie just within the lower limits of
348 the two calibrations. The T and P estimates from the Amp1-Pl2 and Amp2-Pl3 pairs are coincident
349 within error (±50 °C and ±0.2 GPa). This is due to the subtle chemical differences existing between
350 these two generations. Thermobarometric calculations suggest that Pl2 may have grown

351 synchronously with Amp1 at 615°C and 0.97 GPa. The crystallisation of Pl2 marks the first stage of
352 the mylonitic foliation development, as evidenced by the presence of Pl2 in the pressure shadows of
353 Pl1 (Figures 3, 5a and 7). The mylonitic foliation continued to develop under conditions of ~ 600°C
354 and 0.75 GPa (Amp2-Pl3 pair), as supported by the microtextural observation of Amp2, Pl3 and Chl1
355 intergrowths within the Pl1 pressure shadows (Section 4.1). This T result is coincident, within error,
356 with the Chlorite+Quartz+H2O thermometry results for Chl1 (550°C; higher T peak in Figure 6a).

357 The XAn increase from Pl1 to Pl2 and Pl3 could reflect the following reaction from Apted and Liou
358 (1983) for P of 0.7 GPa:

359 epidote + albite + hornblende1 + quartz = oligoclase + hornblende2 + H_2O. (1)

360 The abundant Ep inclusions in Pl1 and its scarcity and corroded aspect in the matrix of the sample
361 would support this hypothesis. Pl2 likely crystallized at temperatures >600°C in the (High-T) Ep-
362 amphibolite facies field (Apted & Liou, 1983; Liou, Kuniyoshi, & Ito, 1974; Miyashiro, 1968;
363 Winkler, 1980), and Pl3 at lower temperatures, as the associated Amp2 and Chl1 limit the maximum
364 T to 550-600°C (Figures 5 and 6a). A final retrograde stage is recorded by the Chl2 compositions
365 suggesting a T range of 350°C-200°C (using the Chlorite+Quartz+H_2O thermometry, Figure 6b), and
366 by the overprinted Chl1 values yielding the low T peak of figure 6a. Indeed, Chl2 appears to be
367 associated with the development of C' shear bands overprinting the mylonitic foliation.

368 **5.2 The origin of luminescence in plagioclase**

369 BSE and CL images provide important insight into feldspar textures (e.g. Lee, Parsons, Edwards, &
370 Martin, 2007; Parsons & Lee, 2009; Parsons, Steele, Lee, & Magee, 2008). Plagioclase luminescence
371 has been related to many causes (summarized in Götze, 2012): the Mn^{2+}, Ti, Fe^{3+} content (Götze,
372 Habermann, Kempe, Neuser, & Richter, 1999; Mariano & King, 1975), trace and REE elements
373 (Götze, Habermann, Neuser, & Richter, 1999; Mariano & King, 1975), lattice defects (e.g. Al-O-Al
374 bridge; Finch & Klein, 1999) and/or mineral inclusions (Smith & Stenstrom, 1965). The CL signal is

375 most commonly linked to Ti concentrations (Lee et al., 2007; Parsons et al., 2008), with a contribution
376 from Fe (Lee et al., 2007). Furthermore, Parsons et al. (2008) has noted that CL emissions appear to
377 be linked to Ca zoning, but they did not find a direct link between Ca concentration (or other trace
378 element concentrations) and CL intensity.

379 In our samples, TiO_2 concentrations appear uniform across all Pl generations (with a content of
380 0.01wt%; Table 2). This is also the case for the MnO concentrations, with a scatter between 0.002
381 and 0.006 wt%. The FeO (Fe total) concentrations in Pl1 and Pl2 are the same (0.03 wt%; Table 2),
382 but increases in Pl3 (0.06 wt%; Table 2). The CL signal in our samples appears to be related to the
383 Ca\Na ratio (with maybe some contribution from Fe): the higher the ratio the brighter the growth
384 zone, as visible from the perfect match between the SEM-CL and EPMA compositional maps
385 (Figures 3 and 7), even though we cannot rule out a contribution from trace and REE elements or
386 lattice defects. Luminescence induced by calcite inclusions in PL2 and 3 can be excluded, as the
387 calcite veins in the sample do not luminesce.

388 **5.3 Replacement reactions by coupled dissolution-precipitation and deformation by**
389 **dissolution-precipitation creep in plagioclase and amphibole**

390 Our analysis highlights a strong correlation between CL images and both BSE images and EPMA
391 compositional maps of plagioclase. Textural and chemical features similar to those reported in this
392 study are recognised in several amphibolites present over > 500 m of the COSC-1 core (from ~1600
393 to ~2300 m deep), implying that the deformation mechanisms and the mineral replacement reactions
394 discussed below are important for the development of the middle to lower crustal thrusts and
395 associated tectonic transport during Caledonian nappe stacking.

396 The plagioclase porphyrocrysts deformation history is summarized in Figure 12a. During the first
397 stage Pl1 grew including a foliation defined by Qz, Ep, Ilm and Rt. Subsequently, fractures developed
398 along the (001) cleavage planes (Ague, 1988; Brander et al., 2012; Brown & Macaudiére, 1984;

399 McLaren & Pryer, 2001) enhanced fluid infiltration that triggered replacement reactions occurring
400 via coupled dissolution of Pl1 and precipitation of Pl2 (Brander et al., 2012; Marti, Stünitz,
401 Heilbronner, Plümper, & Drury, 2017) in equilibrium with the changed P and T conditions of 615°
402 C, 0.9 GPa. These replacement processes continued precipitating Pl3, which rimmed Pl1 and Pl2 and
403 sealed the fractures in Pl1. The slightly different chemistry of Pl3 compared to Pl2 and the
404 microstructural observation that Pl3 overgrows Pl2 suggest that these two growth zones were closely
405 related in time or crystallisation reaction (Section 4.2).

406 The growth zones of Pl2 and Pl3 inherit the crystallographic orientation of the Pl1 cores, with
407 maximum misorientation of 5° (Figure 7c-d). Thus, the precipitation of Pl2 and Pl3 on Pl1 is an
408 example of pseudomorphic and topotaxial growth, as often observed during coupled dissolution-
409 precipitation processes (Engvik et al., 2008; Hövelmann, Putnis, Geisler, Schmidt, & Golla-
410 Schindler, 2010; Plümper et al., 2017; Putnis & Putnis, 2007; Spruzeniece, Piazolo, & Maynard-
411 Casely, 2017). The small (generally < 2°) and only local difference in crystallographic orientation
412 between Pl1 and Pl2-Pl3 presumably results from the slightly different unit cell parameters between
413 albite and oligoclase. The few low angle boundaries associated with Pl2-Pl3 growth zones are
414 typically found along intracrystalline fractures (Figure 7d), and we interpret them as the evidence of
415 slightly rotated fractured fragments of Pl1 that re-equilibrated to Pl2-Pl3 compositions via coupled
416 dissolution-precipitation processes. Pore trails occur in the plagioclase porphyrocrysts parallel to the
417 two fracture systems, together with several micrometric mineral inclusions resulting in a turbid aspect
418 of the plagioclase (Figures 3a-b and 4). Those trails probably represented the main pathways of fluid
419 circulation during coupled Pl1 dissolution and Pl2 and Pl3 precipitation. These mineral inclusions
420 may represent the signature of transient porosity during plagioclase replacement reactions (e.g.
421 Plümper et al., 2017; Plümper & Putnis, 2009; Putnis, 2015; Walker, Lee, & Parsons, 1995).

422 Crystallographic continuity indicative of epitaxial overgrowth is also observed between plagioclase
423 porphyrocrysts and Pl2 and Pl3 grains around them, but to different extents (compare Figure 10a with

Figure 11b). Thus, the crystallographic orientation of new Pl2 and Pl3 grains may be inherited from the Pl1 parent grain due to epitaxy, as described for several minerals deforming by dissolution-precipitation creep at different crustal levels (Engvik et al., 2008; Imon et al., 2002; Imon et al., 2004; Jiang, Prior, & Wheeler, 2000; Mukai et al., 2014; Spruzeniece et al., 2017; Wassmann & Stöckhert, 2012; Wassmann et al., 2011). The crystallographic continuity seems to decrease away from the plagioclase porphyrocrysts (Figures 10b and 11a), presumably reflecting the heterogeneous nucleation of Pl2 and Pl3 neoblasts in the surrounding matrix together with Amp2 and Chl1. Additionally, these neoblasts may have also undergone grain-boundary sliding during deformation, given their fine grain size, which can further disperse their inherited crystallographic orientation (Okudaira et al., 2017).

Thus, we conclude that metamorphism of plagioclase at ~ 600° C and 0.75-0.9 GPa occurred by coupled dissolution-precipitation processes with pseudomorphic and topotaxial replacement of Pl1 by Pl2 and Pl3, and deformation was accommodated by dissolution-precipitation creep with nucleation of Pl2-Pl3 grains around the plagioclase porphyrocrysts (epitaxial) and in the surrounding matrix. It is worth noting that the replacement of Pl1 porphyroclasts by coupled dissolution-precipitation processes generally occurred concentrically (Figure 7). Consequently, at least part of this replacement process outlasted the deformation. The similar chemistry of Pl3 replacing Pl1 and the Pl3 neoblasts in the surrounding matrix suggest that there was no major change in metamorphic conditions throughout the timing of growth of Pl3.

No significant contribution of crystal plasticity was observed, although deformation occurred at PT conditions at which crystal plasticity in plagioclase is expected to occur (e.g. Gerald & Stünitz, 1993;Pearce, Wheeler, & Prior, 2011). The porosity necessary to maintain fluid transport during coupled dissolution-precipitation was generated mostly by fracturing, as shown by the common occurrence of Pl2-Pl3 growth zones along fractures parallel to the (001) perfect cleavage planes. Finally, the sharp chemical transition (across ~1-5 μm) between all the Pl generations, visible from

449 the EPMA and CL maps (Figures 3 and 7), suggest that chemical equilibration did not occur by solid-
450 state diffusion (e.g. Hövelmann et al., 2010).

451 The textural features of amphibole suggest a similar deformation history to plagioclase (Figure 12b).
452 Amp1 (high Mg#) grains are preserved mostly as relict cores and displays embayments, lobate edges
453 and truncated chemical zoning patterns (Figures 3f and 9c; Bukovská, Wirth, & Morales, 2015;
454 Gratier et al., 2013; Hyppolito, García-Casco, Juliani, Meira, & Hall, 2014; Passchier & Trouw, 1996;
455 Rutter, 1983; Stokes et al., 2012; Wassmann & Stöckhert, 2013; Wintsch & Yi, 2002). These textural
456 features suggest that Amp1 underwent coupled dissolution and Amp2 precipitated on Amp1. As for
457 plagioclase, the growth of Amp2 on Amp1 was pseudomorphic and topotaxial (Figure 9d-f). Amp2
458 grew also as smaller neoblasts (maximum few hundreds of μm in size), elongated parallel to the
459 mylonitic foliation and preferentially elongated parallel to their c-axis, due to dissolution-
460 precipitation creep. These crystals do not display Amp1 cores in the compositional maps (Figures 3f
461 and 5b).

462 The CPO and shape-preferred orientation of the amphibole can be acquired via different mechanisms:
463 dissolution-precipitation creep (Bons & den Brok, 2000; Imon et al., 2004; Pearce, Wheeler, & Prior,
464 2011), oriented grain growth and passive rotation after growth (Berger & Stünitz, 1996; Kanagawa,
465 Shimano, & Hiroi, 2008) and/or diffusion creep (Getsinger & Hirth, 2014). In the studied sample the
466 CPO displayed by Amp2 is mostly inherited due to the pseudomorphic and topotaxial growth on
467 Amp1. The small misorientations (< 3°) evident in the EBSD map (Figure 9f) are attributed to
468 fractures that developed perpendicular to the crystal elongation (Figure 9a). Some amphibole crystals
469 display more complex zoning (e.g. central crystal in Figure 9c), probably due to a preferential
470 replacement of the central part of the crystal (e.g. Hyppolito et al., 2014). The CPO of Amp1 grains
471 was presumably formed via oriented grain growth during an earlier deformation event. Moreover, as
472 presented in section 4.6, the misorientation axes of amphibole show maxima around the c-axis, which
473 is oriented subparallel to the stretching lineation of the mylonite (Fig. 11d). This geometry is not

consistent with dislocation creep on the prism <c> slips system of amphibole, as the misorientation axis cannot coincide with the Burgers vector (e.g. Kruse, Stünitz, & Kunze, 2001; Lloyd, Farmer, & Mainprice, 1997). Instead, we interpret the cluster of misorientation axes around <c> as the evidence of topotaxial growth of elongated amphibole grains that preferentially share their c-axis. As the data come from all the grains included in the map (and not only from the rims of Amp2), we think that oriented growth was the dominant deformation mechanisms of amphibole throughout the deformation history.

In the studied sample amphibole, like plagioclase, shows no evidence of deformation via crystal plasticity, such as high intracrystalline misorientations, misorientation bands, subgrains. Instead it appears to have deformed by fracturing and coupled dissolution-precipitation, as also suggested in other studies (Berger & Stünitz, 1996; Brodie & Rutter, 1985; Lafrance & Vernon, 1993; Nyman, Law, & Smelik, 1992; Pearce et al., 2011). Crystal plasticity is potentially a more effective deformation mechanism at higher temperatures (e.g. Skrotzki, 1992).

It is worth noting that the synkinematic reaction that produced Pl2-Pl3 and Amp2 (reaction 1) could have been a dehydration reaction. If this was the case, the aqueous fluid necessary to sustain coupled dissolution-precipitation processes did not necessarily infiltrate from an external source, but may have been released internally. The role of dehydration reactions in the rheological evolution of crustal rocks has received little attention so far, as reaction weakening is commonly associated with hydration reactions during retrogression (e.g. Gueydan, Leroy, Jolivet, & Agard, 2003). However, dehydration reactions that release fluids at grain boundaries can also potentially result in weakening and strain localization during burial and nappe stacking, if the released fluids facilitate the activation of coupled dissolution-precipitation creep and of diffusion creep.

6. CONCLUSIONS

Middle to lower crustal mylonites from the COSC-1 drill core (Lower Seve Nappe) were investigated with EPMA compositional maps, CL images and EBSD maps to constrain the mechanism(s) responsible for their formation. The data suggest that fracturing, coupled dissolution-precipitation and dissolution-precipitation creep were responsible for the development of the mylonitic fabric in amphibolites at conditions of ~600°C, 0.75-0.97 GPa, in the epidote-amphibolite facies, over a thickness of > 500 m. No evidence of deformation via crystal plasticity is present in either plagioclase or amphibole in the analysed sample, even though deformation occurred at pressure and temperature conditions at which plagioclase is expected to deform by dislocation creep. The presence of H_2O-rich fluid at the grain boundaries appears to have enhanced replacement reactions and facilitated dissolution and precipitation processes, which in turn considerably decreased the strength of this middle to lower crustal shear zone. Importantly, replacement reactions of plagioclase only occurred by coupled dissolution-precipitation at grain boundaries and along fractures, and were otherwise sluggish.

Our study shows that crystallographic preferred orientation in plagioclase and amphibole can be inherited from parental grains due to pseudomorphic and topotaxial growth during coupled dissolution-precipitation during deformation. Thus, care must be taken when considering CPOs in deformed rocks as evidence of deformation by dislocation creep.

The development of a mylonitic fabric by coupled dissolution-precipitation and dissolution-precipitation creep in amphibolites over a thickness > 500 in the Lower Seve Nappe suggests that the strength of amphibolites can be significantly low in the presence of grain-boundary aqueous fluid during nappe thrusting in the middle to lower crust.

ACKNOWLEDGEMENTS

Samantha Hammond and Diane Johnson are warmly thanked for the help with EPMA and SEM analyses, respectively. The staff at Plymouth University Electron Microscopy Centre is acknowledged for the support during EBSD analysis. Bjarne Almqvist is acknowledged for his support in acquiring the sample. We acknowledge constructive comments and suggestions from Mark A. Pearce, Robert Wintsch and two anonymous referees that improved the quality of the manuscript. We are grateful to Michael Brown for editorial handling.

This work was funded by an Early Postdoc.Mobility funding scheme (project number: P2BEP2_168722) granted by Swiss National Science Foundation. LM acknowledges financial support from a FP7 Marie Curie Career Integration Grant (grant agreement PCIG13-GA-2013-618289).

REFERENCES

Ague, D. M. (1988). Universal stage measurements and transmission electron microscope observations of fractured plagioclase. *Journal of Structural Geology, 10*(7), 701-705.

Anderson, J. L., Barth, A. P., Wooden, J. L., & Mazdab, F. (2008). Thermometers and thermobarometers in granitic systems. *Reviews in Mineralogy and Geochemistry, 69*(1), 121-142.

Anderson, J. L., & Smith, D. R. (1995). The effects of temperature and fO_2 on the Al-in-hornblende barometer. *American Mineralogist, 80*(5-6), 549-559.

Andréasson, P. (1994). The Baltoscandian margin in Neoproterozoic-early Palaeozoic times. Some constraints on terrane derivation and accretion in the Arctic Scandinavian Caledonides. *Tectonophysics, 231*(1-3), 1-32.

Apted, M. J., & Liou, J. (1983). Phase relations among greenschist, epidote-amphibolite, and amphibolite in a basaltic system. *American Journal of Science, 283*, 328-354.

Arnbom, J.-O. (1980). Metamorphism of the Seve Nappes at Åreskutan, Swedish Caledonides. *Geologiska Föreningen i Stockholm Förhandlingar, 102*(4), 359-371. doi:10.1080/11035898009454493

Berger, A., & Stünitz, H. (1996). Deformation mechanisms and reaction of hornblende: examples from the Bergell tonalite (Central Alps). *Tectonophysics, 257*(2), 149-174.

Bergman, S., & Sjöström, H. (1997). Accretion and lateral extension in an orogenic wedge: evidence from a segment of the Seve-Ko¨li terrane boundary, central Scandinavian Caledonides. *Journal of Structural Geology, 19*(8), 1073-1091. doi:http://dx.doi.org/10.1016/S0191-8141(97)00028-X

Bhadra, S., & Bhattacharya, A. (2007). The barometer tremolite+ tschermakite+ 2 albite= 2 pargasite+ 8 quartz: Constraints from experimental data at unit silica activity, with application to garnet-free natural assemblages. *American Mineralogist, 92*(4), 491-502.

556 Bons, P. D., & den Brok, B. (2000). Crystallographic preferred orientation development by
557 dissolution–precipitation creep. *Journal of Structural Geology, 22*(11), 1713-1722.
558 Brander, L., Svahnberg, H., & Piazolo, S. (2012). Brittle-plastic deformation in initially dry rocks at
559 fluid-present conditions: transient behaviour of feldspar at mid-crustal levels. *Contributions*
560 *to Mineralogy and Petrology, 163*(3), 403-425.
561 Brodie, K., & Rutter, E. (1985). On the relationship between deformation and metamorphism, with
562 special reference to the behavior of basic rocks. In *Metamorphic reactions* (pp. 138-179):
563 Springer.
564 Brown, W. L., & Macaudiére, J. (1984). Microfracturing in relation to atomic structure of plagioclase
565 from a deformed meta-anorthosite. *Journal of Structural Geology, 6*(5), 579-586.
566 Brueckner, H. K., & van Roermund, H. L. (2004). Dunk tectonics: a multiple subduction/eduction
567 model for the evolution of the Scandinavian Caledonides. *Tectonics, 23*(2).
568 Brueckner, H. K., & Van Roermund, H. L. (2007). Concurrent HP metamorphism on both margins
569 of Iapetus: Ordovician ages for eclogites and garnet pyroxenites from the Seve Nappe
570 Complex, Swedish Caledonides. *Journal of the Geological Society, 164*(1), 117-128.
571 Bukovská, Z., Wirth, R., & Morales, L. F. (2015). Pressure solution in rocks: focused ion
572 beam/transmission electron microscopy study on orthogneiss from South Armorican Shear
573 Zone, France. *Contributions to Mineralogy and Petrology, 170*(3), 31.
574 Bürgmann, R., & Dresen, G. (2008). Rheology of the lower crust and upper mantle: Evidence from
575 rock mechanics, geodesy, and field observations. *Annual Review of Earth and Planetary*
576 *Sciences, 36*.
577 Carmichael, D. M. (1969). On the mechanism of prograde metamorphic reactions in quartz-bearing
578 pelitic rocks. *Contributions to Mineralogy and Petrology, 20*(3), 244-267.
579 Engvik, A. K., Putnis, A., Gerald, J. D. F., & Austrheim, H. (2008). Albitization of granitic rocks: the
580 mechanism of replacement of oligoclase by albite. *The Canadian Mineralogist, 46*(6), 1401-
581 1415.
582 Finch, A. A., & Klein, J. (1999). The causes and petrological significance of cathodoluminescence
583 emissions from alkali feldspars. *Contributions to Mineralogy and Petrology, 135*(2-3), 234-
584 243.
585 Fusseis, F., & Handy, M. (2008). Micromechanisms of shear zone propagation at the brittle–viscous
586 transition. *Journal of Structural Geology, 30*(10), 1242-1253.
587 Fusseis, F., Regenauer-Lieb, K., Liu, J., Hough, R., & De Carlo, F. (2009). Creep cavitation can
588 establish a dynamic granular fluid pump in ductile shear zones. *Nature, 459*(7249), 974-977.
589 Gayer, R., Rice, A., Roberts, D., Townsend, C., & Welbon, A. (1987). Restoration of the Caledonian
590 Baltoscandian margin from balanced cross-sections: the problem of excess continental crust.
591 *Transactions of the Royal Society of Edinburgh: Earth Sciences, 78*(03), 197-217.
592 Gee, D. (1975). A tectonic model for the central part of the Scandinavian Caledonides. *American*
593 *Journal of Science, 275*(A), 468-515.
594 Gee, D., Fossen, H., Henriksen, N., & Higgins, A. K. (2008). From the early Paleozoic platforms of
595 Baltica and Laurentia to the Caledonide Orogen of Scandinavia and Greenland. *Episodes,*
596 *31*(1), 44-51.
597 Gee, D., Janák, M., Majka, J., Robinson, P., & van Roermund, H. (2013). Subduction along and
598 within the Baltoscandian margin during closing of the Iapetus Ocean and Baltica-Laurentia
599 collision. *Lithosphere, 5*(2), 169-178.
600 Gee, D., Juhlin, C., Pascal, C., & Robinson, P. (2010). Collisional orogeny in the Scandinavian
601 Caledonides (COSC). *Gff, 132*(1), 29-44.
602 Gee, D., & Sturt, B. (1985). *The Caledonide orogen: Scandinavia and related areas* (Vol. 2): Wiley.
603 Gerald, J. F., & Stünitz, H. (1993). Deformation of granitoids at low metamorphic grade. I: Reactions
604 and grain size reduction. *Tectonophysics, 221*(3), 269-297.
605 Getsinger, A., & Hirth, G. (2014). Amphibole fabric formation during diffusion creep and the
606 rheology of shear zones. *Geology, 42*(6), 535-538.

607 Gilio, M., Clos, F., & van Roermund, H. L. (2015). The Friningen Garnet Peridotite (central Swedish
608 Caledonides). A good example of the characteristic PTt path of a cold mantle wedge garnet
609 peridotite. *Lithos, 230*, 1-16.
610 Gilotti, J. A. (1989). Reaction progress during mylonitization of basaltic dikes along the Särv thrust,
611 Swedish Caledonides. *Contributions to Mineralogy and Petrology, 101*(1), 30-45.
612 Giuntoli, F., Lanari, P., & Engi, M. (2018). Deeply subducted continental fragments – Part 1:
613 Fracturing, dissolution–precipitation, and diffusion processes recorded by garnet textures of
614 the central Sesia Zone (western Italian Alps). *Solid Earth, 9*(1), 167-189. doi:10.5194/se-9-
615 167-2018
616 Götze, J. (2012). Application of cathodoluminescence microscopy and spectroscopy in geosciences.
617 *Microscopy and Microanalysis, 18*(06), 1270-1284.
618 Götze, J., Habermann, D., Kempe, U., Neuser, R. D., & Richter, D. K. (1999). Cathodoluminescence
619 microscopy and spectroscopy of plagioclases from lunar soil. *American Mineralogist, 84*(7-
620 8), 1027-1032.
621 Götze, J., Habermann, D., Neuser, R. D., & Richter, D. K. (1999). High-resolution spectrometric
622 analysis of rare earth elements-activated cathodoluminescence in feldspar minerals. *Chemical
623 Geology, 153*(1), 81-91.
624 Gratier, J.-P., Dysthe, D. K., & Renard, F. (2013). The role of pressure solution creep in the ductility
625 of the Earth's upper crust. *Advances in Geophysics, 54*, 47-179.
626 Grimmer, J. C., Glodny, J., Drüppel, K., Greiling, R. O., & Kontny, A. (2015). Early-to mid-Silurian
627 extrusion wedge tectonics in the central Scandinavian Caledonides. *Geology, 43*(4), 347-350.
628 Gueydan, F., Leroy, Y. M., Jolivet, L., & Agard, P. (2003). Analysis of continental midcrustal strain
629 localization induced by microfracturing and reaction-softening. *Journal of Geophysical
630 Research: Solid Earth, 108*(B2).
631 Hedin, P., Almqvist, B., Berthet, T., Juhlin, C., Buske, S., Simon, H., . . . Alm, P.-G. (2016). 3D
632 reflection seismic imaging at the 2.5 km deep COSC-1 scientific borehole, central
633 Scandinavian Caledonides. *Tectonophysics, 689*, 40-55.
634 Holland, T., & Blundy, J. (1994). Non-ideal interactions in calcic amphiboles and their bearing on
635 amphibole-plagioclase thermometry. *Contributions to Mineralogy and Petrology, 116*(4),
636 433-447.
637 Hövelmann, J., Putnis, A., Geisler, T., Schmidt, B. C., & Golla-Schindler, U. (2010). The replacement
638 of plagioclase feldspars by albite: observations from hydrothermal experiments.
639 *Contributions to Mineralogy and Petrology, 159*(1), 43-59.
640 Hyppolito, T., García-Casco, A., Juliani, C., Meira, V., & Hall, C. (2014). Late Paleozoic onset of
641 subduction and exhumation at the western margin of Gondwana (Chilenia Terrane):
642 Counterclockwise P–T paths and timing of metamorphism of deep-seated garnet–mica schist
643 and amphibolite of Punta Sirena, Coastal Accretionary Complex, central Chile (34 S). *Lithos,
644 206*, 409-434.
645 Imon, R., Okudaira, T., & Fujimoto, A. (2002). Dissolution and precipitation processes in deformed
646 amphibolites: an example from the ductile shear zone of the Ryoke metamorphic belt, SW
647 Japan. *Journal of Metamorphic Geology, 20*(3), 297-308.
648 Imon, R., Okudaira, T., & Kanagawa, K. (2004). Development of shape-and lattice-preferred
649 orientations of amphibole grains during initial cataclastic deformation and subsequent
650 deformation by dissolution–precipitation creep in amphibolites from the Ryoke metamorphic
651 belt, SW Japan. *Journal of Structural Geology, 26*(5), 793-805.
652 Jackson, J., Austrheim, H., McKenzie, D., & Priestley, K. (2004). Metastability, mechanical strength,
653 and the support of mountain belts. *Geology, 32*(7), 625-628.
654 Janák, M., van Roermund, H., Majka, J., & Gee, D. (2013). UHP metamorphism recorded by kyanite-
655 bearing eclogite in the Seve Nappe Complex of northern Jämtland, Swedish Caledonides.
656 *Gondwana Research, 23*(3), 865-879.

Jiang, Z., Prior, D. J., & Wheeler, J. (2000). Albite crystallographic preferred orientation and grain misorientation distribution in a low-grade mylonite: implications for granular flow. *Journal of Structural Geology, 22*(11), 1663-1674.

Kanagawa, K., Shimano, H., & Hiroi, Y. (2008). Mylonitic deformation of gabbro in the lower crust: A case study from the Pankenushi gabbro in the Hidaka metamorphic belt of central Hokkaido, Japan. *Journal of Structural Geology, 30*(9), 1150-1166.

Klonowska, I., Janák, M., Majka, J., Froitzheim, N., & Kośmińska, K. (2016). Eclogite and garnet pyroxenite from Stor Jougdan, Seve Nappe Complex, Sweden: implications for UHP metamorphism of allochthons in the Scandinavian Caledonides. *Journal of Metamorphic Geology, 34*(2), 103-119.

Klonowska, I., Janák, M., Majka, J., Petrík, I., Froitzheim, N., Gee, D., & Sasinková, V. (2017). Microdiamond on Åreskutan confirms regional UHP metamorphism in the Seve Nappe Complex of the Scandinavian Caledonides. *Journal of Metamorphic Geology*.

Kruse, R., Stünitz, H., & Kunze, K. (2001). Dynamic recrystallization processes in plagioclase porphyroclasts. *Journal of Structural Geology, 23*(11), 1781-1802.

Ladenberger, A., Be'eri-Shlevin, Y., Claesson, S., Gee, D. G., Majka, J., & Romanova, I. V. (2013). Tectonometamorphic evolution of the Åreskutan Nappe–Caledonian history revealed by SIMS U–Pb zircon geochronology. *Geological Society, London, Special Publications, 390*, SP390. 310.

Lafrance, B., & Vernon, R. (1993). Mass transfer and microfracturing in gabbroic mylonites of the Guadalupe igneous complex, California. *Defects and processes in the solid state: geoscience applications: the McLaren volume (Developments in Petrology, Vol. 4). Amsterdam, Elsevier Science*, 151-167.

Lanari, P. (2012). *Micro-cartographie P-T-e dans les roches métamorphiques. Applications aux Alpes et à l'Himalaya.* (Doctorate PhD), Grenoble,

Lanari, P., Guillot, S., Schwartz, S., Vidal, O., Tricart, P., Riel, N., & Beyssac, O. (2012). Diachronous evolution of the alpine continental subduction wedge: evidence from P-T estimates in the Briançonnais Zone houillere (France – Western Alps). *Journal of Geodynamics, 56-57*, 39-54.

Lanari, P., Riel, N., Guillot, S., Vidal, O., Schwartz, S., Pêcher, A., & Hattori, K. H. (2013). Deciphering high-pressure metamorphism in collisional context using microprobe mapping methods: Application to the Stak eclogitic massif (northwest Himalaya). *Geology, 41*(2), 111-114.

Lanari, P., Vidal, O., Lewin, E., Dubacq, B., De Andrade, V., & Schwartz, S. (2014). XMapTools a Matlab©-based graphic user interface for microprobe quantified image processing. *Computers and Geosciences, 62*, 227-240. doi:10.1016/j.cageo.2013.08.010

Leake, B. E., Woolley, A. R., Arps, C. E., Birch, W. D., Gilbert, M. C., Grice, J. D., . . . Krivovichev, V. G. (1997). Report. Nomenclature of Amphiboles: Report of the Subcommittee on Amphiboles of the International Mineralogical Association Commission on New Minerals and Mineral Names. *Mineralogical Magazine, 61*(2), 295-321.

Lee, M. R., Parsons, I., Edwards, P. R., & Martin, R. W. (2007). Identification of cathodoluminescence activators in zoned alkali feldspars by hyperspectral imaging and electron-probe microanalysis. *American Mineralogist, 92*(2-3), 243-253.

Liou, J., Kuniyoshi, S., & Ito, K. (1974). Experimental studies of the phase relations between greenschist and amphibolite in a basaltic system. *American Journal of Science, 274*(6), 613-632.

Lloyd, G. E., Farmer, A. B., & Mainprice, D. (1997). Misorientation analysis and the formation and orientation of subgrain and grain boundaries. *Tectonophysics, 279*(1-4), 55-78.

Lorenz, H., Rosberg, J.-E., Juhlin, C., Bjelm, L., Almqvist, B. S. G., Berthet, T., . . . Pascal, C. (2015). COSC-1-drilling of a subduction-related allochthon in the Palaeozoic Caledonide orogen of Scandinavia. *Scientific Drilling, 19*, 1.

Majka, J., Rosén, Å., Janák, M., Froitzheim, N., Klonowska, I., Manecki, M., . . . Yoshida, K. (2014). Microdiamond discovered in the Seve Nappe (Scandinavian Caledonides) and its exhumation by the "vacuum-cleaner" mechanism. *Geology, 42*(12), 1107-1110.

Mariano, A., & King, P. (1975). Europium-activated cathodoluminescence in minerals. *Geochimica et Cosmochimica Acta, 39*(5), 649-660.

Marti, S., Stünitz, H., Heilbronner, R., Plümper, O., & Drury, M. (2017). Experimental investigation of the brittle-viscous transition in mafic rocks–Interplay between fracturing, reaction, and viscous deformation. *Journal of Structural Geology, 105*, 62-79.

McAleer, R., Bish, D., Kunk, M., Sicard, K., Valley, P., Walsh, G., . . . Wintsch, R. (2017). Reaction softening by dissolution–precipitation creep in a retrograde greenschist facies ductile shear zone, New Hampshire, USA. *Journal of Metamorphic Geology, 35*(1), 95-119.

McLaren, A., & Pryer, L. (2001). Microstructural investigation of the interaction and interdependence of cataclastic and plastic mechanisms in feldspar crystals deformed in the semi-brittle field. *Tectonophysics, 335*(1), 1-15.

Menegon, L., Fusseis, F., Stünitz, H., & Xiao, X. (2015). Creep cavitation bands control porosity and fluid flow in lower crustal shear zones. *Geology, 43*(3), 227-230.

Menegon, L., Pennacchioni, G., & Spiess, R. (2008). Dissolution-precipitation creep of K-feldspar in mid-crustal granite mylonites. *Journal of Structural Geology, 30*(5), 565-579.

Miyashiro, A. (1968). Metamorphism of mafic rocks. *Basalts, 2*, 799-834.

Mouthereau, F., Lacombe, O., & Vergés, J. (2012). Building the Zagros collisional orogen: timing, strain distribution and the dynamics of Arabia/Eurasia plate convergence. *Tectonophysics, 532*, 27-60.

Mouthereau, F., Watts, A. B., & Burov, E. (2013). Structure of orogenic belts controlled by lithosphere age. *Nature Geosci, 6*(9), 785-789. doi:10.1038/ngeo1902

http://www.nature.com/ngeo/journal/v6/n9/abs/ngeo1902.html#supplementary-information

Mukai, H., Austrheim, H., Putnis, C. V., & Putnis, A. (2014). Textural evolution of plagioclase feldspar across a shear zone: implications for deformation mechanism and rock strength. *Journal of Petrology, 55*(8), 1457-1477.

Newton, R. C., & Smith, J. (1967). Investigations concerning the breakdown of albite at depth in the earth. *The Journal of Geology, 75*(3), 268-286.

Northrup, C. (1996). Structural expressions and tectonic implications of general noncoaxial flow in the midcrust of a collisional orogen: The northern Scandinavian Caledonides. *Tectonics, 15*(2), 490-505.

Nyman, M. W., Law, R. D., & Smelik, E. A. (1992). Cataclastic deformation mechanism for the development of core-mantle structures in amphibole. *Geology, 20*(5), 455-458.

Okudaira, T., Shigematsu, N., Harigane, Y., & Yoshida, K. (2017). Grain size reduction due to fracturing and subsequent grain-size-sensitive creep in a lower crustal shear zone in the presence of a CO2-bearing fluid. *Journal of Structural Geology, 95*, 171-187. doi:https://doi.org/10.1016/j.jsg.2016.11.001

Parsons, I., & Lee, M. R. (2009). Mutual replacement reactions in alkali feldspars I: microtextures and mechanisms. *Contributions to Mineralogy and Petrology, 157*(5), 641.

Parsons, I., Steele, D. A., Lee, M. R., & Magee, C. W. (2008). Titanium as a cathodoluminescence activator in alkali feldspars. *American Mineralogist, 93*(5-6), 875-879.

Passchier, C., & Trouw, R. (1996). Microtectonics: Springer Verlag. *Berlin, Germany*, 289.

Pearce, M. A., Wheeler, J., & Prior, D. J. (2011). Relative strength of mafic and felsic rocks during amphibolite facies metamorphism and deformation. *Journal of Structural Geology, 33*(4), 662-675.

Plümper, O., Botan, A., Los, C., Liu, Y., Malthe-Sørenssen, A., & Jamtveit, B. (2017). Fluid-driven metamorphism of the continental crust governed by nanoscale fluid flow. *Nature Geoscience, 10*, 685. doi:10.1038/ngeo3009

https://www.nature.com/articles/ngeo3009#supplementary-information
Plumper, O., John, T., Podladchikov, Y. Y., Vrijmoed, J. C., & Scambelluri, M. (2017). Fluid escape from subduction zones controlled by channel-forming reactive porosity. *Nature Geosci, 10*(2), 150-156. doi:10.1038/ngeo2865

http://www.nature.com/ngeo/journal/v10/n2/abs/ngeo2865.html#supplementary-information
Plümper, O., & Putnis, A. (2009). The complex hydrothermal history of granitic rocks: multiple feldspar replacement reactions under subsolidus conditions. *Journal of Petrology, 50*(5), 967-987.
Prior, D. J., Wheeler, J., Peruzzo, L., Spiess, R., & Storey, C. (2002). Some garnet microstructures: an illustration of the potential of orientation maps and misorientation analysis in microstructural studies. *Journal of Structural Geology, 24*(6), 999-1011.
Putnis, A. (2002). Mineral replacement reactions: from macroscopic observations to microscopic mechanisms. *Mineralogical Magazine, 66*(5), 689-708.
Putnis, A. (2009). Mineral replacement reactions. *Reviews in Mineralogy and Geochemistry, 70*(1), 87-124.
Putnis, A. (2015). Transient porosity resulting from fluid–mineral interaction and its consequences. *Reviews in Mineralogy and Geochemistry, 80*, 1-23.
Putnis, A., & Putnis, C. V. (2007). The mechanism of reequilibration of solids in the presence of a fluid phase. *Journal of Solid State Chemistry, 180*(5), 1783-1786.
Rice, A. H. N., & Anderson, M. W. (2016). Restoration of the external Scandinavian Caledonides. *Geological Magazine*, 1-30.
Roberts, D. (2003). The Scandinavian Caledonides: event chronology, palaeogeographic settings and likely modern analogues. *Tectonophysics, 365*(1), 283-299.
Roberts, D., & Gee, D. (1985). An introduction to the structure of the Scandinavian Caledonides. *The Caledonide orogen–Scandinavia and related areas, 1*, 55-68.
Root, D., & Corfu, F. (2012). U–Pb geochronology of two discrete Ordovician high-pressure metamorphic events in the Seve Nappe Complex, Scandinavian Caledonides. *Contributions to Mineralogy and Petrology, 163*(5), 769-788.
Royden, L. (1996). Coupling and decoupling of crust and mantle in convergent orogens: Implications for strain partitioning in the crust. *Journal of Geophysical Research: Solid Earth, 101*(B8), 17679-17705.
Ruiz-Agudo, E., Putnis, C., & Putnis, A. (2014). Coupled dissolution and precipitation at mineral–fluid interfaces. *Chemical Geology, 383*, 132-146.
Rutter, E. (1983). Pressure solution in nature, theory and experiment. *Journal of the Geological Society, 140*(5), 725-740.
Rutter, E., & Brodie, K. (1992). Rheology of the lower crust. *Continental lower crust*, 201-267.
Sjöström, H. (1983). The Seve—Köli Nappe Complex of the Handöl—Storlien—Essandsjøen area, Scandinavian Caledonides. *Geologiska Föreningen i Stockholm Förhandlingar, 105*(2), 93-117.
Skrotzki, W. (1992). Defect structure and deformation mechanisms in naturally deformed hornblende. *physica status solidi (a), 131*(2), 605-624.
Smith, J., & Stenstrom, R. (1965). Electron-excited luminescence as a petrologic tool. *The Journal of Geology, 73*(4), 627-635.
Spruzeniece, L., Piazolo, S., & Maynard-Casely, H. E. (2017). Deformation-resembling microstructure created by fluid-mediated dissolution–precipitation reactions. *Nature Communications, 8*, 14032.
Stephens, M. B. (1988). The Scandinavian Caledonides: a complexity of collisions. *Geology Today, 4*(1), 20-26.

Stokes, M., Wintsch, R., & Southworth, C. (2012). Deformation of amphibolites via dissolution–precipitation creep in the middle and lower crust. *Journal of Metamorphic Geology, 30*(7), 723-737.

Strand, T., & Kulling, O. (1972). *Scandinavian Caledonides*: John Wiley & Sons.

Strömberg, A., Karis, L., Zachrisson, E., Sjöstrand, T., Skoglund, R., Lundegårdh, P., . . . Kornfält, K. (1984). Berggrundskarta över Jämtlands län utom förutvarande Fjällsjö kommun, scale 1: 200 000. *Geological Survey of Sweden, Ca, 53*.

Tullis, J., Yund, R., & Farver, J. (1996). Deformation-enhanced fluid distribution in feldspar aggregates and implications for ductile shear zones. *Geology, 24*(1), 63-66.

Van Roermund, H. (1985). Eclogites of the Seve nappe, central Scandinavian Caledonides. *The Caledonide Orogen—Scandinavia and Related Areas*, 873-886.

Van Roermund, H. (1989). High-pressure ultramafic rocks from the allochthonous nappes of the Swedish Caledonides. *The Caledonide Geology of Scandinavia*, 205-219.

Vidal, O., De Andrade, V., Lewin, E., Munoz, M., Parra, T., & Pascarelli, S. (2006). P–T-deformation-Fe3+/Fe2+ mapping at the thin section scale and comparison with XANES mapping: application to a garnet-bearing metapelite from the Sambagawa metamorphic belt (Japan). *Journal of Metamorphic Geology, 24*(7), 669-683.

Vidal, O., Lanari, P., Munoz, M., Bourdelle, F., & De Andrade, V. (2016). Deciphering temperature, pressure and oxygen-activity conditions of chlorite formation. *Clay Minerals, 51*(4), 615-633.

Vidal, O., Parra, T., & Vieillard, P. (2005). Thermodynamic properties of the Tschermak solid solution in Fe-chlorite: Application to natural examples and possible role of oxidation. *American Mineralogist, 90*(2-3), 347-358.

Walker, F. D. L., Lee, M. R., & Parsons, I. (1995). Micropores and micropermeable texture in alkali feldspars: geochemical and geophysical implications. *Mineralogical Magazine, 59*(3), 505-534.

Wallis, D., Phillips, R., & Lloyd, G. (2014). Evolution of the Eastern Karakoram Metamorphic Complex, Ladakh, NW India, and its relationship to magmatism and regional tectonics. *Tectonophysics, 626*, 41-52.

Wassmann, S., & Stöckhert, B. (2012). Matrix deformation mechanisms in HP-LT tectonic mélanges—microstructural record of jadeite blueschist from the Franciscan Complex, California. *Tectonophysics, 568*, 135-153.

Wassmann, S., & Stöckhert, B. (2013). Rheology of the plate interface—dissolution precipitation creep in high pressure metamorphic rocks. *Tectonophysics, 608*, 1-29.

Wassmann, S., Stöckhert, B., & Trepmann, C. A. (2011). Dissolution precipitation creep versus crystalline plasticity in high-pressure metamorphic serpentinites. *Geological Society, London, Special Publications, 360*(1), 129-149.

Wenning, Q. C., Berthet, T., Ask, M., Zappone, A., Rosberg, J. E., & Almqvist, B. S. (2017). Image log analysis of in situ stress orientation, breakout growth, and natural geologic structures to 2.5 km depth in central Scandinavian Caledonides: Results from the COSC-1 borehole. *Journal of Geophysical Research: Solid Earth*.

Whitney, D. L., & Evans, B. W. (2010). Abbreviations for names of rock-forming minerals. *American Mineralogist, 95*(1), 185-187.

Winkler, W. (1980). Petrogenesis of metamorphic rocks, 5th ed. *Springer-Verlag, New York*(1), 348 p.

Wintsch, R., & Yi, K. (2002). Dissolution and replacement creep: a significant deformation mechanism in mid-crustal rocks. *Journal of Structural Geology, 24*(6), 1179-1193.

Zachrisson, E., & Sjöstrand, T. (1990). Bedrock Map 22E Frostviken. *Sveriges Geologiska Undersökning (SGU) Ai 44, scale 1: 50,000*.

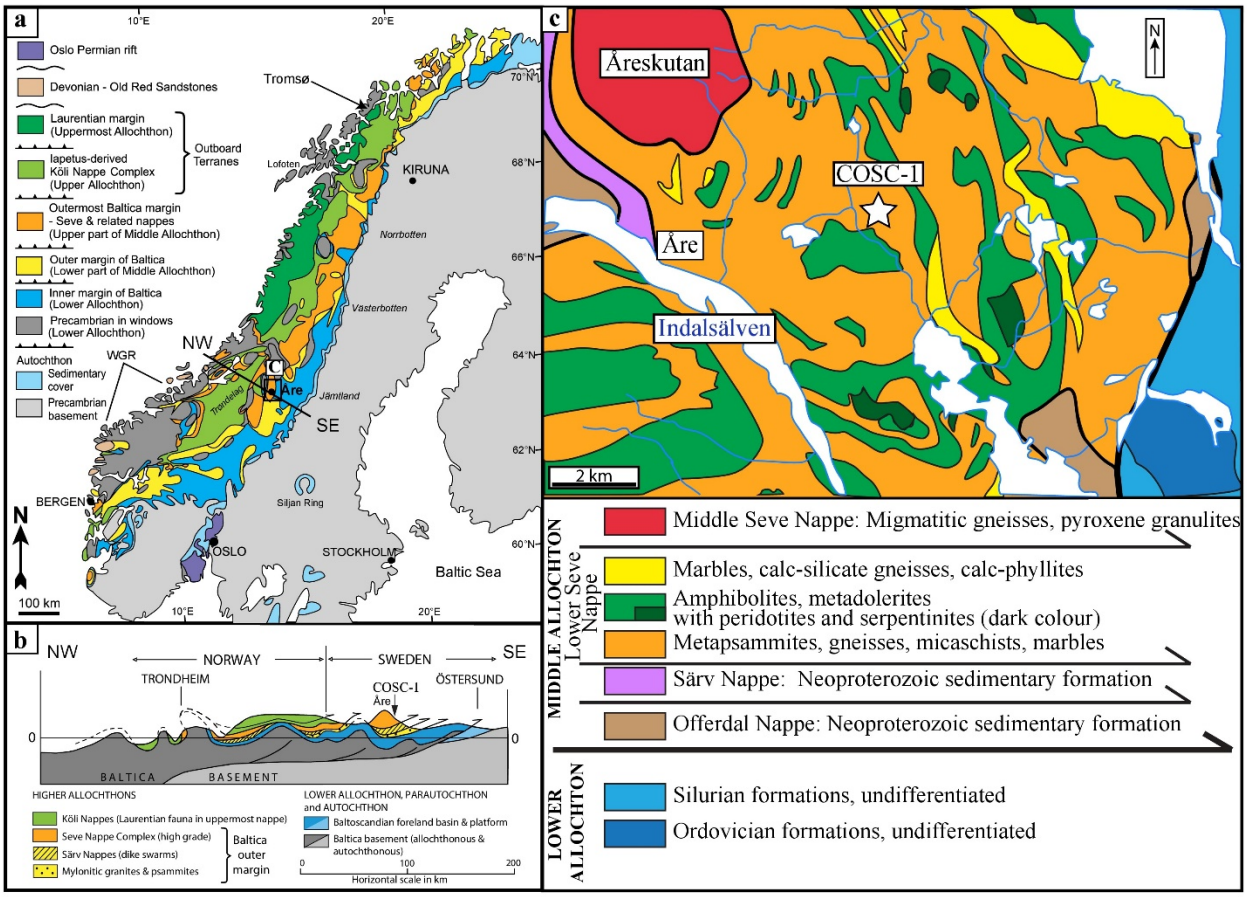

855

856 **FIGURE 1** Geological setting of the Scandinavian Caledonides. (a) Tectonic map with inferred
857 paleogeography of the nappes (modified after Gee et al., 2010). (b) Cross section marked in (a) with
858 vertical exaggeration of 5 x and approximate location of the COSC-1 borehole (modified after Gee
859 et al., 2010). (c) Detail of the study area with location of the COSC-1 drilling site (modified after
860 Strömberg et al., 1984).

861

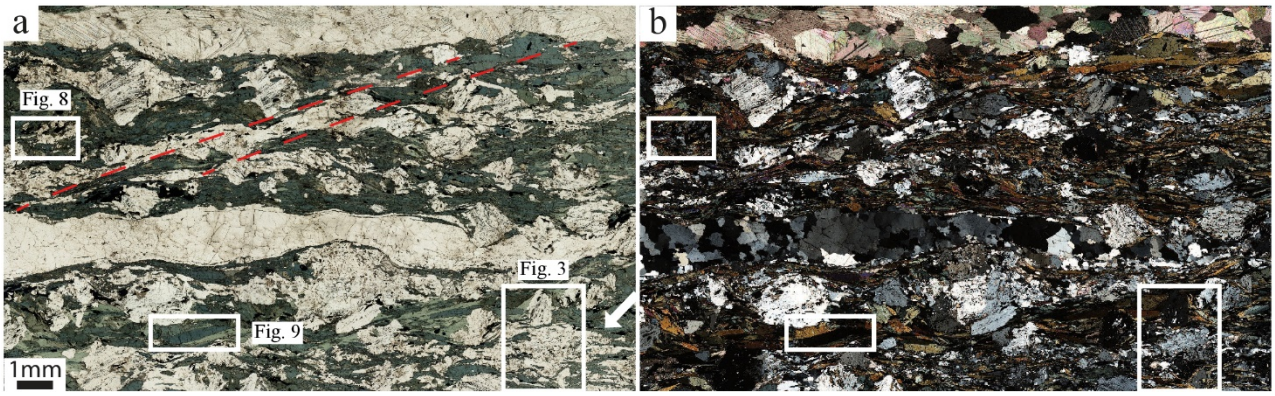

862

863 **FIGURE 2** Amphibolite with Pl porphyroclast displaying a mylonitic foliation defined by Amp, Pl,
864 Chl, Qz, Ep and Ilm. Cal and Qz ribbons, presumably representing transposed veins, are parallel to
865 the foliation. Both dextral- (clasts close to Figure 3 rectangle, marked by the white arrow) and sinistral
866 sense of shear (C' planes, red dashed line) are visible. (a): *plane-polarized light*; (b): *crossed-*
867 *polarized light*. Mineral abbreviation from Whitney and Evans (2010).

Minerals	**Pre-main foliation**	**Main foliation**	**C' Planes**
Amp	– – – –	———	
Pl	Ab Core ———	Ab/Olig Rims ———	
Chl		———	– – – –
Quartz	———	———	– – – –
Cal	– – – –	———	– – – –
Epidote	———	– – – –	
Ilmenite	———	———	

868 **TABLE 1:** Metamorphic and deformation evolution of sample ICDP5054EX8E601.

869

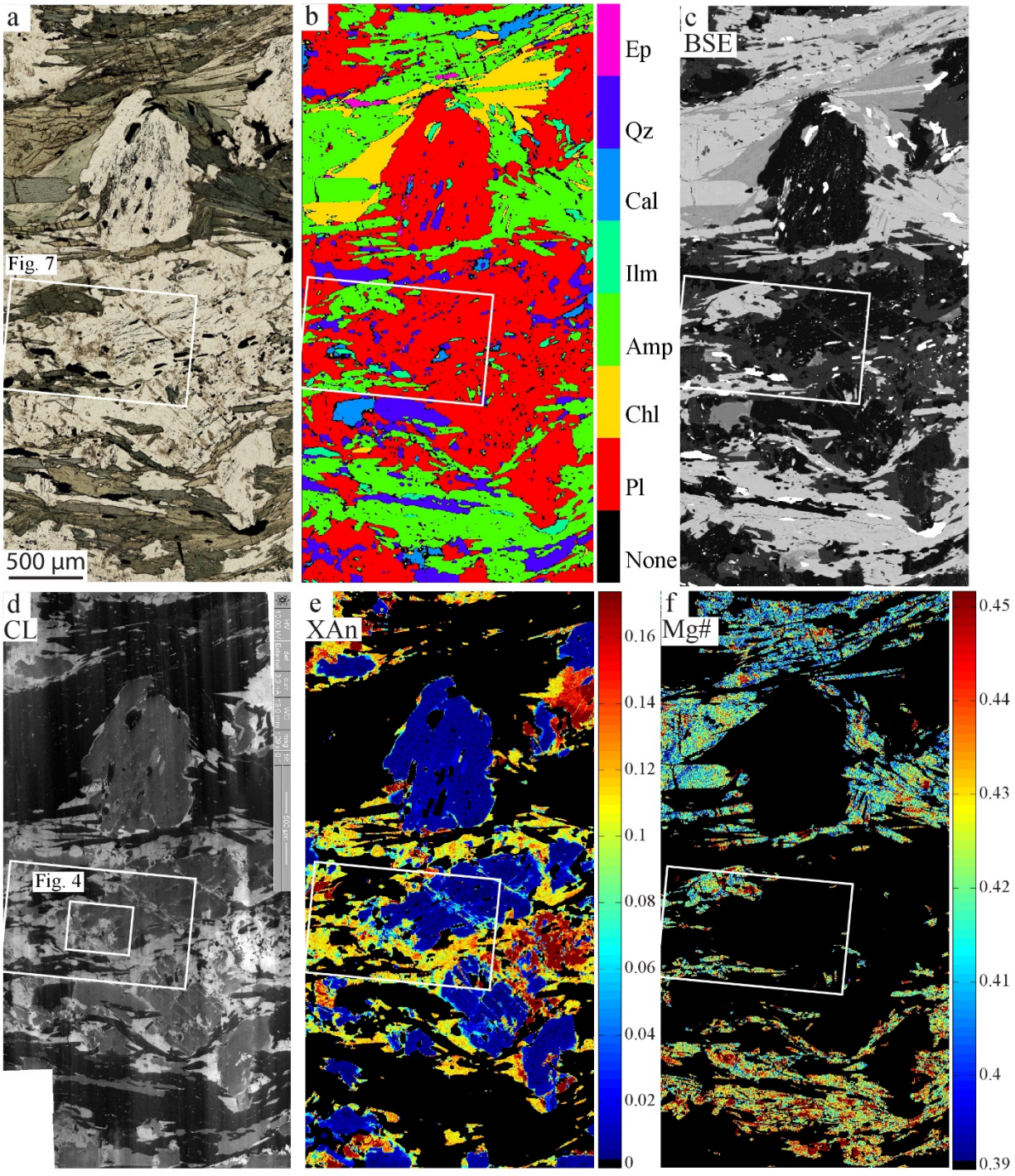

870

871 **FIGURE 3** More detailed areas of sections shown in Figure 2. (a) Ab porphyroclasts with dark trails
872 of inclusions of Ep and Cal few µm in size. The Ab porphyroclasts are wrapped by the mylonitic
873 foliation defined by Amp, Olig and Chl. The white rectangle indicates the site of the EBSD map
874 shown in Figure 7 (*plane polarized light*). (b) X-ray map showing Pl, Amp, Chl and Ep that crystallize
875 in the pressure shadows of Ab porphyroclasts. (c) BSE image showing zoned Pl with dark cores (Pl1)
876 and brighter rims (Pl2 and Pl3). Bright inclusions inside Pl are Ilm crystals. (d) CL image highlighting

the difference between Ab cores (dark, Pl1) rimmed by Pl with higher An content (bright, Pl2 and Pl3). This bright Pl crystallises also in the pressure shadows and in the fractures that dissect the Ab cores. (e) Standardized X-Ray map of the X Anorthite (XAn) in the Pl. Note the fractures in Pl1 sealed by Pl3 and sheared-off fragments of Pl1 rimmed by Pl2 and 3 (see text and Figure 5 for distinction). (f) Standardized X-Ray map of Amp crystals displaying relic cores higher in Mg# (Amp1) and rims lower in Mg# lengthened as the main foliation (Amp2). A minor but consistent shift toward higher Mg# is visible from the top to the bottom of the picture, probably related to an analytical artefact.

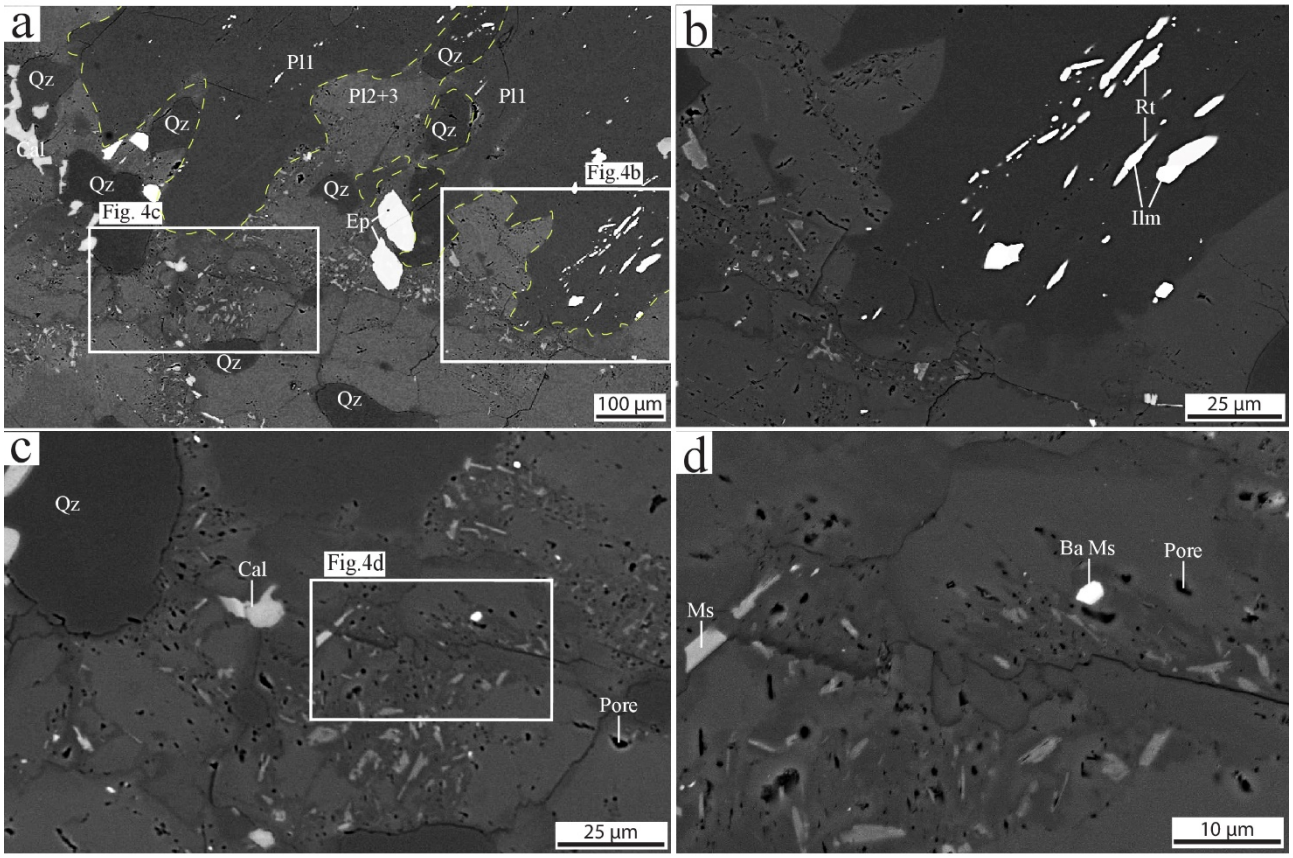

FIGURE 4 Details of the microstructures shown in Figure 3c. BSE images. (a) Dark Pl1, highlighted by the dashed yellow line, with lobate edges and peninsular features rimmed by Pl2 and Pl3. (b) Iso-oriented Ilm and Rt inclusions in Pl1. Note the two perpendicular trails of pores in Pl2 and Pl3. (c) Detail of the pore trails and associated Ms and Cal inclusions. (d) Close-up of (c) highlighting pores, abundant Ms inclusions and rare Ba-rich Ms.

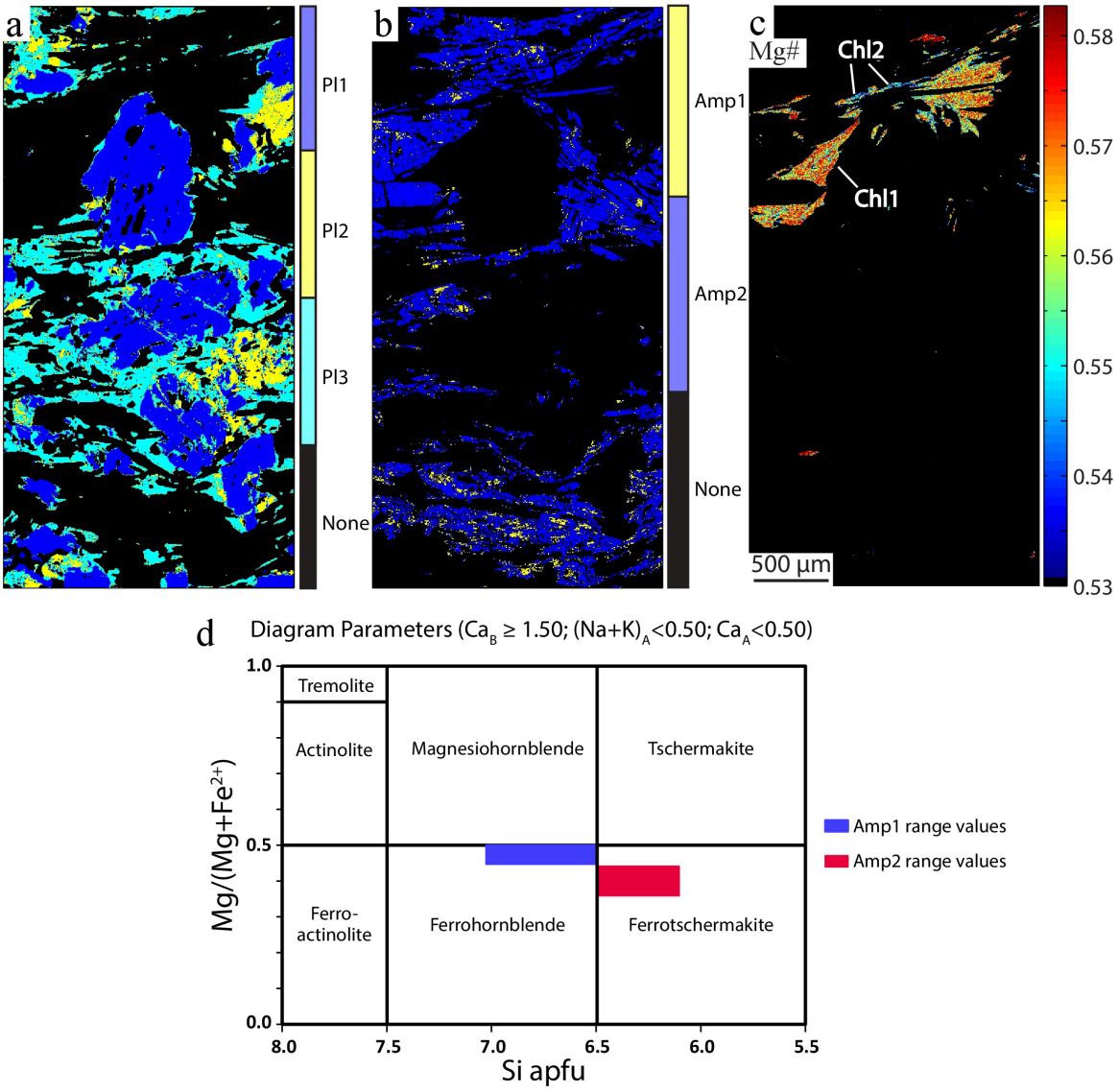

891

892 **FIGURE 5** Mineral chemistry of Pl, Amp and Chl. The subdivision in generations was made based
893 on microtextures. (a) Pl groups based on the XAb and XAn content: Pl1 XAn 0-0.05; Pl2 XAn 0.05-
894 0.13; Pl3 XAn 0.13-0.25. Compare with Figure 3e. (b) Amp groups based on the Mg# and Si apfu
895 content: Amp1 Mg# 0.5-0.44, Si apfu 7-6.5; Amp2 Mg# 0.44-0.36, Si apfu 6.5-6.1. Compare with
896 Figure 3f. (c) Compositional map of Chl Mg# for 0% Fe^{3+}. The crystals display homogeneous
897 compositions (Chl1 Mg# 0.59-0.56), except at grain boundaries and along C' band where lower
898 values are present (Chl2 Mg# 0.55-0.52) (d) Diagram of classification of calcic amphiboles with
899 plotted the average chemical compositions of Amp1 and Amp2 (from Leake et al., 1997).

900

	Pl			Amp	
	Core (Pl1)	Rim1 (Pl2)	Rim2 (Pl3)	Core (Amp1)	Rim (Amp2)
SiO2	68.21	62.95	64.99	43.52	41.62
TiO2	0.01	0.01	0.01	0.22	0.35
Al2O3	19.08	24.37	21.55	13.21	15.42
FeO	0.03	0.03	0.06	18.41	18.56
MnO	0.00	0.00	0.00	0.17	0.17
MgO	0.00	0.00	0.00	8.34	7.37
CaO	0.11	4.30	2.30	11.42	10.72
Na2O	12.34	8.93	10.47	1.72	2.02
K2O	0.04	0.05	0.05	0.21	0.35
Sum	99.83	100.64	99.43	97.22	96.57
	Formulae based on 8 O			**Formulae based on 23 anhydrous O**	
Si	2.99	2.76	2.88	6.49	6.26
Ti	-	-	-	0.02	0.04
Al	0.99	1.26	1.12	2.33	2.73
Fe^{3+}	-	-	-	0.41	0.49
Fe^{2+}	-	-	-	1.89	1.85
Mn	-	-	-	0.02	0.02
Mg	-	-	-	1.86	1.65
Ca	0.01	0.20	0.11	1.83	1.73
Na	1.05	0.76	0.90	0.50	0.59
K	0.00	0.00	0.00	0.04	0.07
Sum	5.04	4.99	5.01	15.38	15.42
Mg#	-	-	-	0.45	0.41
XAn	0.01	0.21	0.11	-	-
XAb	0.99	0.79	0.89	-	-

901 **TABLE 2** Representative average composition analysis (wt%) of Pl and Amp.

902

Chl	Chl1-High Mg#		Chl2-Low Mg#	
	0% XFe^{3+}	30% XFe^{3+}	0% XFe^{3+}	30% XFe^{3+}
SiO2	25.70	25.70	26.52	26.69
Al2O3	22.33	22.34	21.70	21.69
FeO	22.00	21.98	22.60	22.41
Fe2O3	-	0.02	-	0.21
MnO	0.15	0.15	0.15	0.14
MgO	16.43	16.43	15.37	15.42
CaO	0.02	0.02	0.03	0.03
Na2O	0.01	0.01	0.01	0.02
K2O	0.00	0.00	0.01	0.01
Sum	86.63	86.65	86.38	86.62
Formulae based on 14 anhydrous O				
Si	2.69	2.63	2.78	2.74
Al	2.75	2.70	2.68	2.62
Mg	2.56	2.51	2.41	2.36
Fe^{3+}	0.00	0.57	0.00	0.58
Fe^{2+}	1.92	1.32	1.98	1.35
Sum	9.92	9.73	9.85	9.65
Mg#	0.57	0.66	0.55	0.64

903 **TABLE 3** Representative average composition analysis (wt%) of Chl.

904

Amp-Pl couples	Thermometer	Barometer	
	HB	BB	AS
Amp1-Pl1	**392 °C**	-	-
Amp1-Pl2	**615 °C**	**0.97 GPa**	0.87 GPa
Amp2-Pl3	**605 °C**	**0.74 GPa**	1.09 GPa

905

906 **TABLE 4** Results of Amphibole-Plagioclase geothermobarometry computed from the values of
907 Table 2. Thermometer abbreviation: HB: Holland and Blundy (1994). Barometer abbreviations: BB:
908 Bhadra and Bhattacharya (2007); AS: Anderson and Smith (1995). The favoured results are
909 highlighted in bold (see Section 5.1 for details).

910

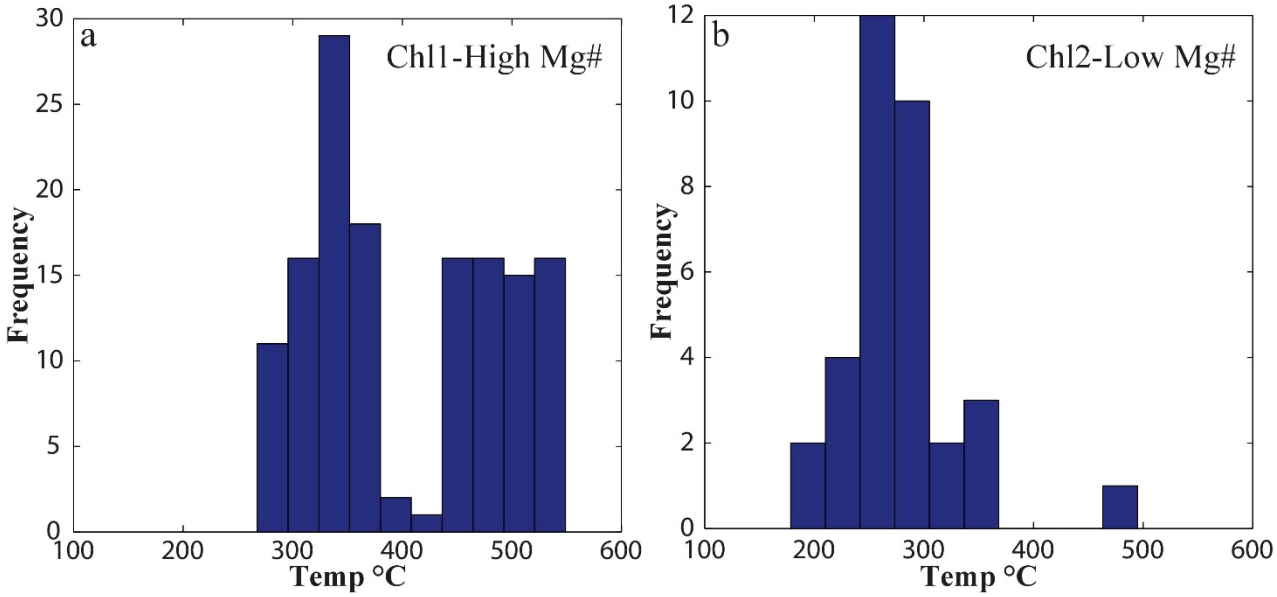

911

912 **FIGURE 6** Chlorite+Quartz+H_2O thermometry results calculated at a pressure of 0.7 GPa and a

913 range between 0-50 % of Fe^{3+}.

914

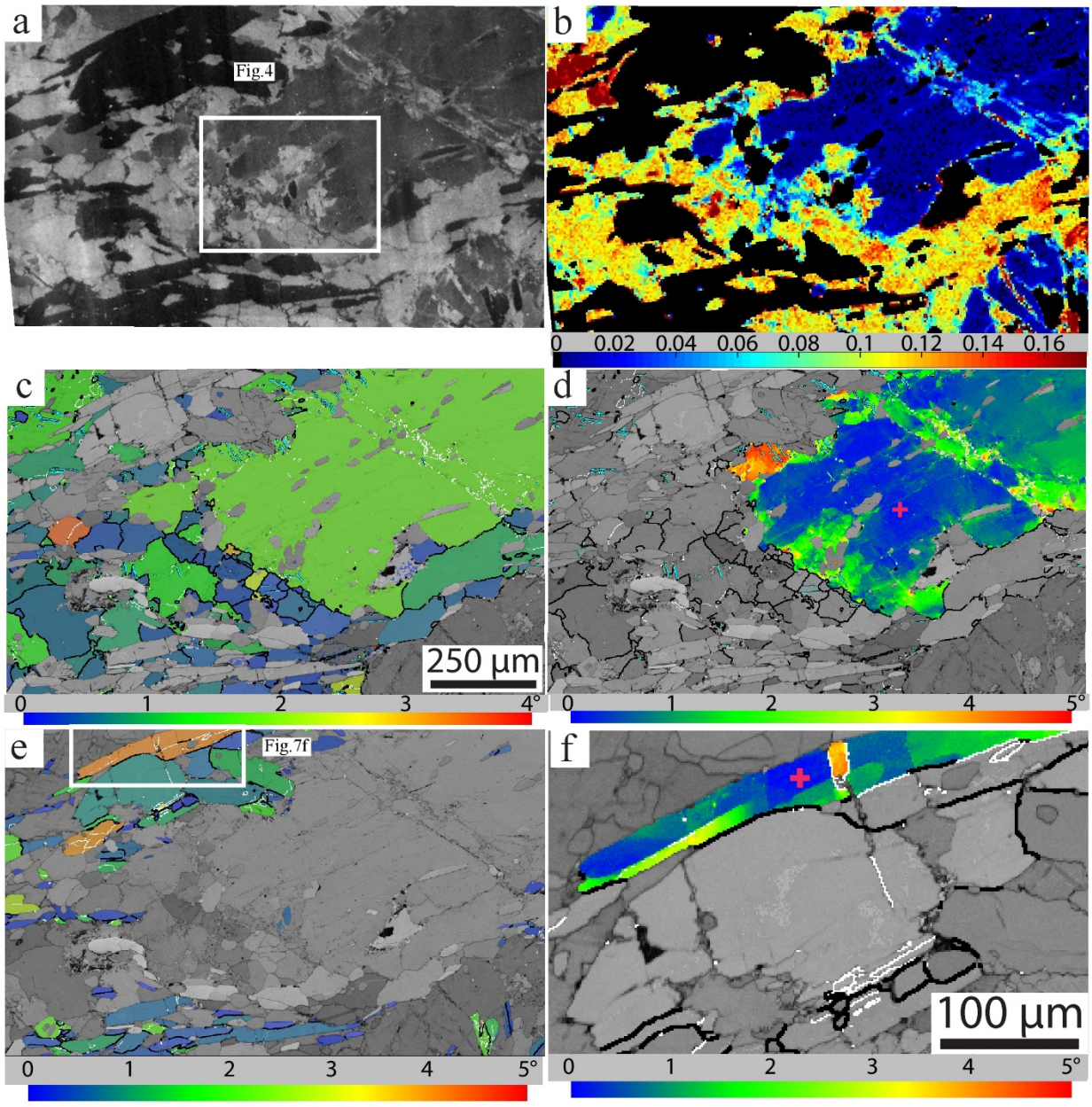

915

916 **FIGURE 7** Details of the microstructure shown in Figure 3 (referred to as domain 1 in the text). (a)
917 CL image of a dark Pl1 porphyroclast with fractures and rims containing the bright Pl2-3. (b)
918 Standardized X-Ray map of the XAn content showing the overlap between the bright CL areas and
919 the Pl2-Pl3 compositions. (c) EBSD GOS map superposed to the band contrast (BC) map of the same
920 area shown in (a). White lines: low angle boundaries 2-10°. Black lines: high angle boundaries > 10°.
921 Light blue lines: Twin boundaries in Pl. (d) EBSD texture component map (TCM) of the Pl1
922 porphyroclast, showing the misorientation from the reference point marked by the red cross. White
923 lines: low angle boundaries 2-10°. Black lines: high angle boundaries > 10°. Light blue lines: Twin

924 boundaries in Pl. (e) EBSD GOS of Amp from the area shown in (a). White lines: low angle
925 boundaries 2-10°. Black lines: high angle boundaries > 10°. (f) EBSD TCM of Amp, showing the
926 misorientation from the reference point marked by the red cross. White lines: low angle boundaries
927 2-10°. Black lines: high angle boundaries > 10°.

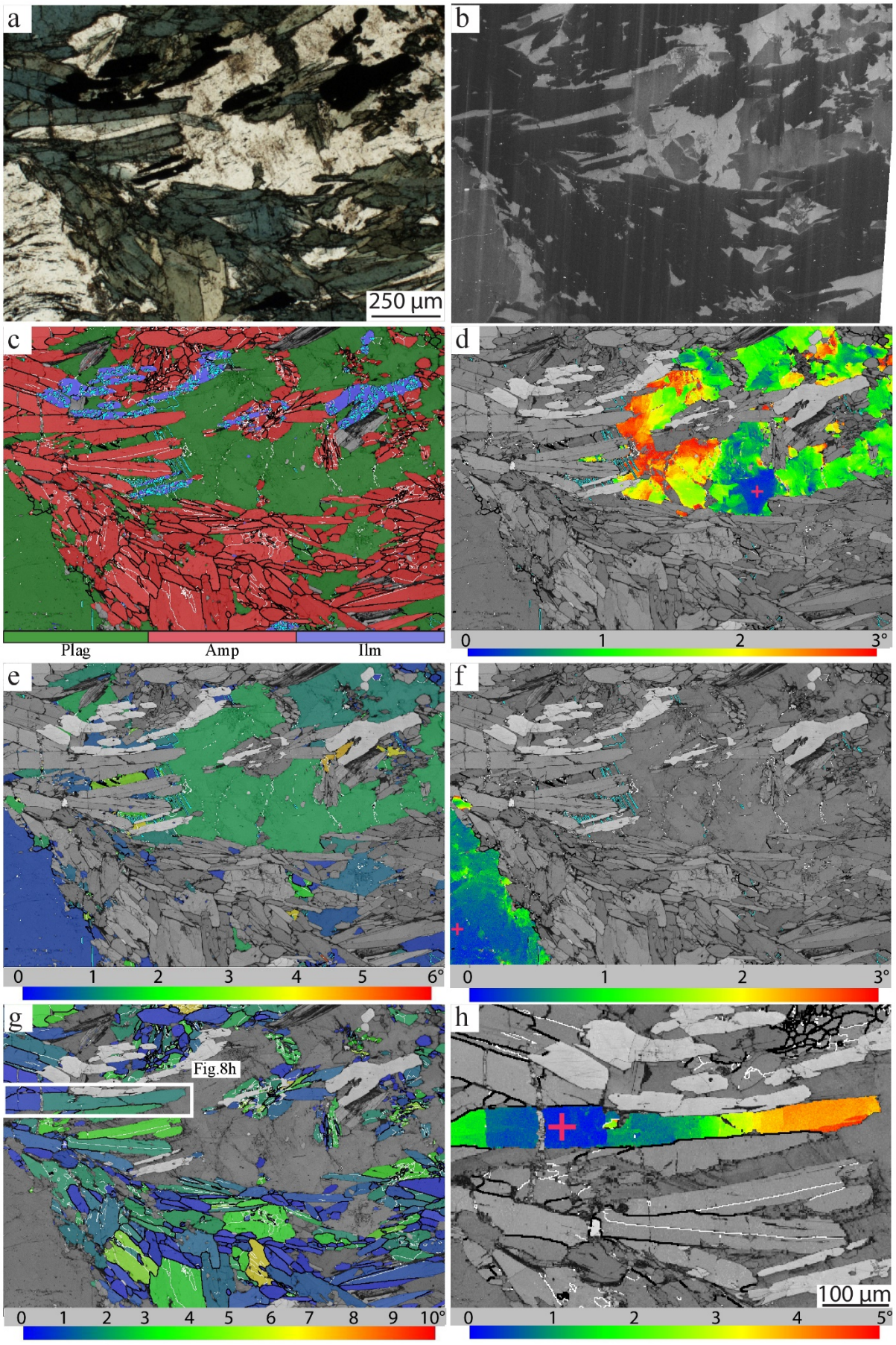
a
250 µm
b
c
Plag
Amp
Ilm
d
0 1 2 3°
e
0 1 2 3 4 5 6°
f
0 1 2 3°
g
Fig.8h
0 1 2 3 4 5 6 7 8 9 10°
h
100 µm
0 1 2 3 4 5°

928

FIGURE 8 Details of Figure 2 (referred to as domain 2 in the text). (a) Light microscopy microstructure of the site analysed with EBSD. (b) CL image of the site shown in (a). Dark Pl1 porphyroclasts are overgrown by bright Pl2 and Pl3. (c) EBSD phases map of the site shown in (a). Note the epitaxial growth of Pl2 and Pl3 on Pl1, as indicated by the lack of high angle boundaries separating Pl1 from Pl2 and Pl3, and the very few low angle boundaries in the Pl1 porphyroclast. (d) EBSD TCM showing the misorientation from reference point (red cross) in Pl1 porphyroclasts. Note the correlation between higher misorientation and Pl2-Pl3 overgrowth on the right-hand side of the reference point. (e) EBSD GOS map suggesting that the Pl crystals are very low internal strain. (f) EBSD TCM showing the misorientation from reference point of another Pl1 porphyroclast. (g) EBSD GOS map of Amp. (h) EBSD TCM showing the misorientation from reference point in an Amp crystal elongate parallel to the foliation.

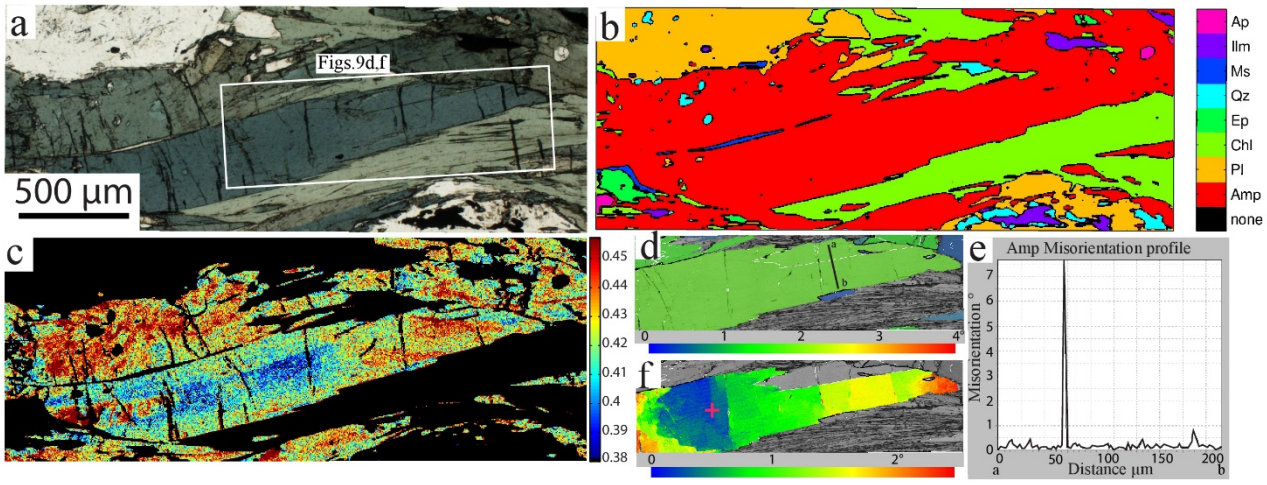

FIGURE 9 Details of Figure 2. (a) Sigmoidal grain of Amp surrounded by Chl along the foliation wrapping around Pl porphyroclasts. Several brittle fractures perpendicular to the Amp elongation are visible (*plane-polarized light*). The white rectangle encompasses the site of the EBSD maps shown in (d) and (f). (b) X-ray map of the mineral phases in (a). (c) Standardized X-Ray map showing the variation in Mg# of Amp grains (scale bar on the right-hand side). Amp displays cores higher in Mg# (Amp1) and rims lower in Mg# (Amp2) elongate parallel to the foliation (compare with Figure 3f).

948 (d) EBSD GOS map of Amp. The black line is the trace of the misorientation profile a-b shown in
949 (e). See (a) for the location of the map. (e) Misorientation profile a-b drawn across a low-angle
950 boundary. (f) EBSD TCM showing the misorientation from the reference point marked by a red cross.

951

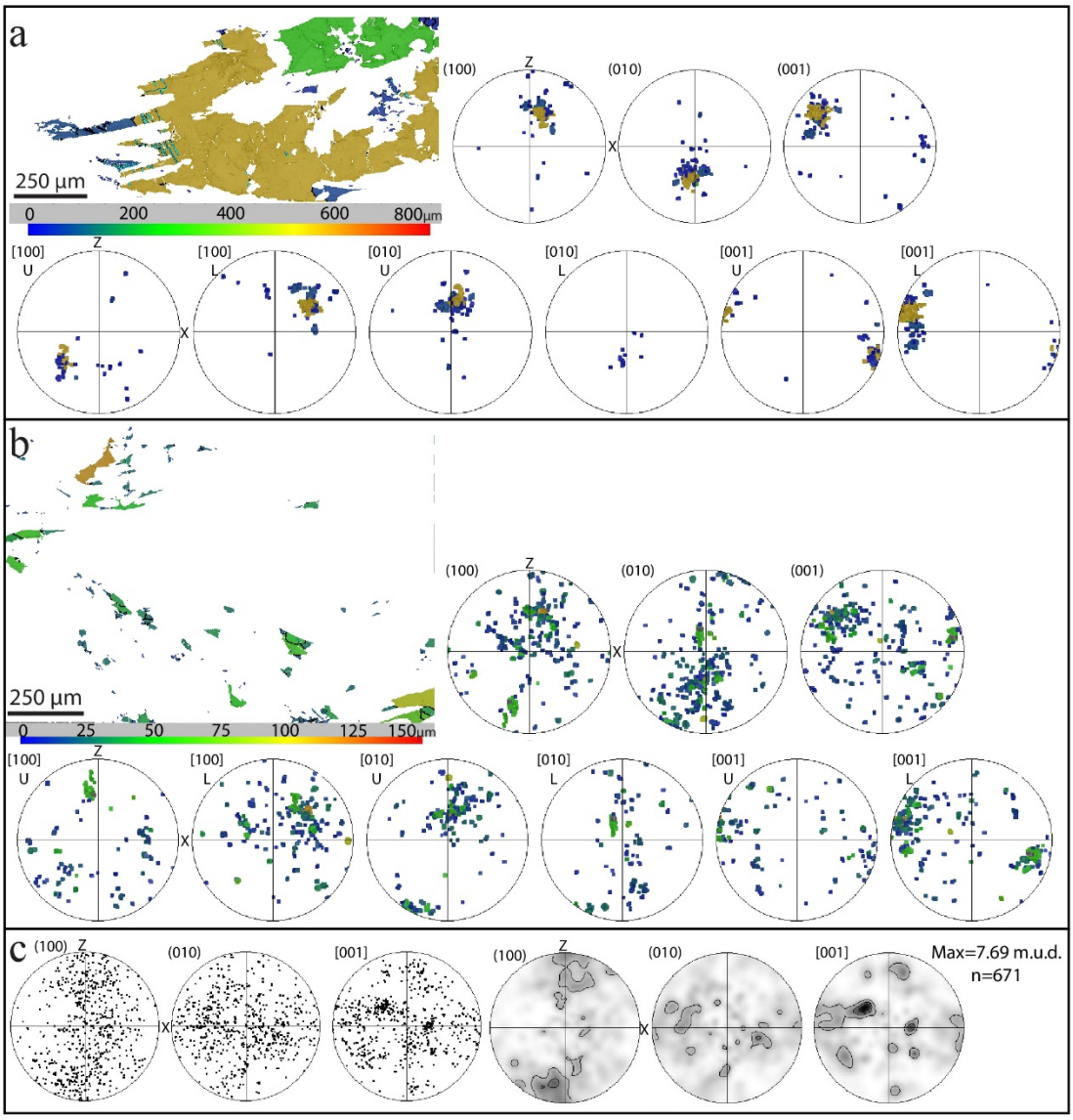

952

953 **FIGURE 10** Pole figures of the crystallographic orientation data of Pl (colour-coding as in the grain
954 size maps) and Amp; same site as maps shown in Figure 8. X is the extensional instantaneous
955 stretching axis, Z is the pole of foliation, stereographic projections, lower hemisphere if not specified;
956 U: upper hemisphere, L: lower hemisphere. (a) Subset of the Pl porphyroclast and adjacent grains
957 sharing the same crystallographic orientation, with the exception of a few data points. The Pl displays

a CPO with the (100) and (001) maxima approximately at 45° from X. The (010) maximum is perpendicular to X. a: 189029 Pl data points. (b) Subset of the Pl crystals of the matrix (Pl2 and 3) not adjacent to the porphyroclast. A weak CPO similar to Figure 11a is visible. 34676 Pl data points. (c) Amp displaying a CPO with the (100) and [001] perpendicular and parallel to X, respectively. 671 Amp data points (one-point-per-grain). n=number of grains. Half width 10° and cluster size 5°, maximum value is given. Contouring is 1.

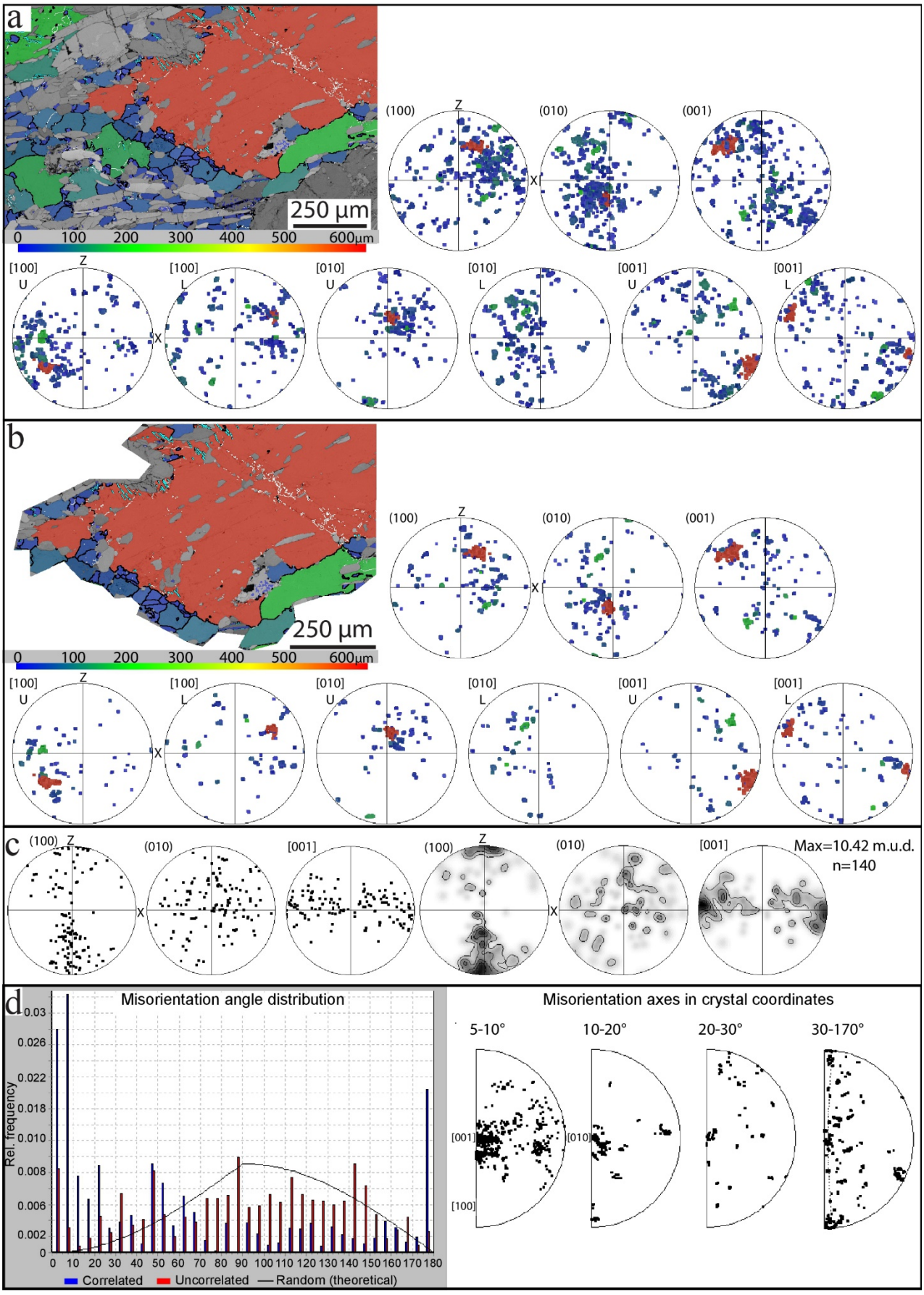
a
250 µm
0 100 200 300 400 500 600µm
(100) Z
(010)
(001)
X
[100] U
[100] L
[010] U
[010] L
[001] U
[001] L
b
250 µm
0 100 200 300 400 500 600µm
c
(100) Z
(010)
[001]
Max=10.42 m.u.d.
n=140
d
Misorientation angle distribution
Rel. frequency
0 0.002 0.006 0.008 0.010 0.018 0.022 0.026 0.03
0 10 20 30 40 50 60 70 80 90 100 110 120 130 140 150 160 170 180
Correlated
Uncorrelated
Random (theoretical)
Misorientation axes in crystal coordinates
5-10°
10-20°
20-30°
30-170°
[001]
[010]
[100]

FIGURE 11 Pole figures of the crystallographic orientation data of Pl (colour-coding as in the grain size maps) and Amp; same site as maps shown in Figure 7. (a) The Pl displays a CPO with the (100) and (001) at low to medium angles to X. Note how the maximum of the values coincides with the porphyroclast values, in red. 357353 Pl data points. (b) Subset of the Pl porphyroclast and adjacent grains; some of the latter display a similar crystallographic orientation as the porphyroclast. 238333 Pl data points (c) Pole figures of Amp displaying a strong CPO with the (100) and [001] perpendicular and parallel to X, respectively. 140 Amp data points (one-point-per-grain). n=number of grains. Half width 10° and cluster size 5°, maximum value is given. Contouring is 2. (d) Histogram of distribution of misorientation angles and misorientation axes of amphibole plotted in crystal coordinates. 3295 Amp data points. Dashed line: forbitten zone limit.

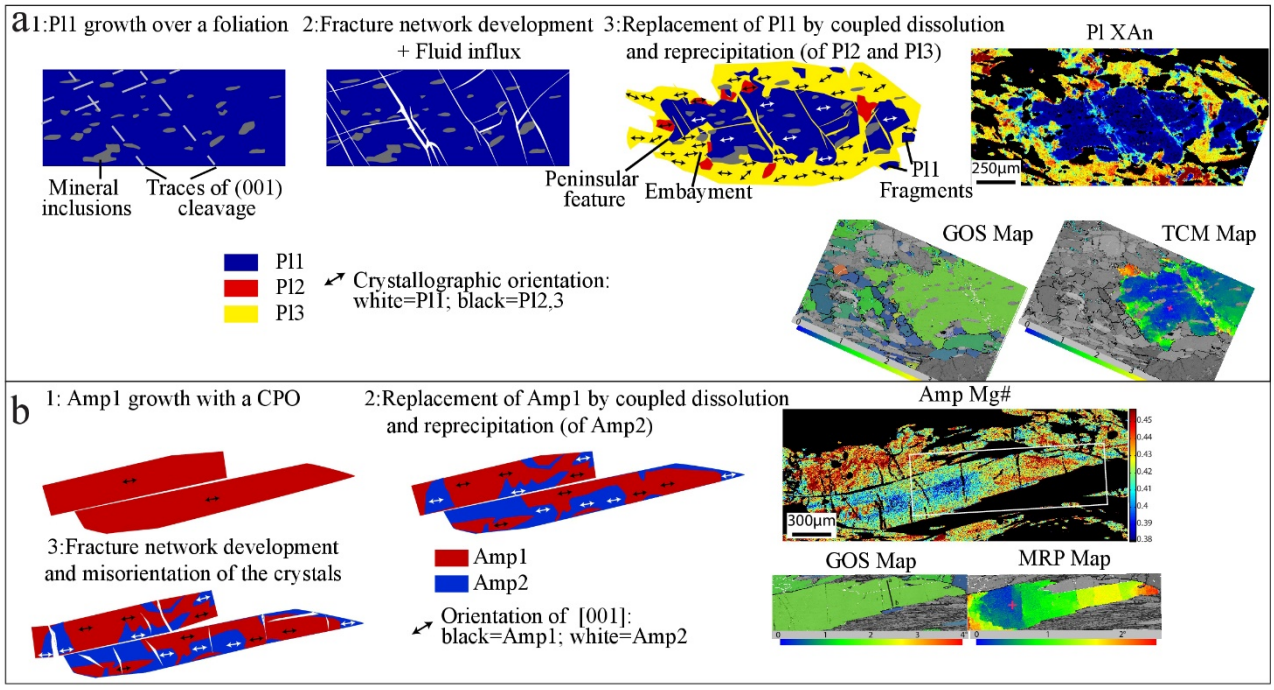

FIGURE 12 Idealized sketch of the deformation history of Pl and Amp, colour-coding as in the compositional maps. (a) 1: Pl1 porphyrocrysts grew including a foliation marked by Ep, Qz and Ilm. 2: Fracturing of the Pl1 porphyrocrysts, mostly imposed along the (001) plane. 3: Fluid infiltration triggered mineral replacement by coupled dissolution-precipitation with topotaxial and

pseudomorphic growth of Pl2 and, successively, Pl3 on Pl1. Replacement occurred mostly along and in proximity of the fractures as well as at the edges of the crystals. Pl3 nucleated also as newly grown grains in the matrix. (b) 1: Amp1 grew with a CPO. 2: Replacement of Amp1 by Amp2 by coupled dissolution-precipitation; topotaxial growth is suggested by the same CPO shared by the two generations. 3: Development of misorientation due to displacement along the fractures and along the cleavage planes.